University of Alberta

Measurements of Radiation Induced Currents in RF Coil Conductors

by

Andrei Dorin Ghila

A thesis submitted to the Faculty of Graduate Studies and Research
in partial fulfillment of the requirements for the degree of

Master of Science

In

Medical Physics

Department of Oncology

Fall 2011
Edmonton, Alberta

Abstract

The integration of a clinical linear accelerator (linac) with a magnetic resonance imager (MRI) will offer real time images during treatment, making tumor tracking possible. One of the challenges of the integration is removing any mutual interference between the two systems. Methods of removing or significantly reducing the radiation induced current (RIC) that appears in the MRI's radio frequency (RF) coils when they are under the linac's direct pulsed irradiation are investigated in this thesis. The results indicate that by using the proper combination of coil conductor and buildup the RIC can be reduced to negligible levels. This was demonstrated on a custom built surface RF coil as well. A preliminary investigation of how having an RF coil with or without buildup in the treatment beam will affect the patient's skin dose was also done. Future measurements to determine whether the measured RIC in RF coils significantly affects the quality of the acquired images are suggested.

Acknowledgement

I would like to thank my supervisor Dr. Satyapal Rathee, for all his guidance during the completion of this work. Thank you for all our discussions, for your open door policy, for promptly responding to my emails, and for keeping me on track with my work.

Also I would like to thank Dr. Gino Fallone for being the driving force behind this great project and for allowing me to be part of the team. Your advice, your to the point comments and your no bull policy makes us all strive to be better physicists and better scientists.

Many thanks to my project partner, Ben Burke, for all his patience with me at the beginning, while showing me the ropes. Thank you for all your advice, and for being there when I needed to discuss my ideas with someone.

To my parents, thank you both for your support, for encouraging me to keep on with my studies, and generally for still putting up with me after all these years.

Table of Contents

List of Figures

List of Abbreviations

ART	Adaptive Radiation Treatment
CBCT	Cone Beam Computed Tomography
CPE	Charged Particle Equilibrium
CRT	Conformal Radiation Therapy
CT	Computed Tomography
EPID	Electronic Portal Imaging Device
ICRU	International Commission on Radiation Units
IGRT	Image Guided Radiation Therapy
IMRT	Intensity Modulated Radiation Therapy
kV	Kilovoltage
linac	Linear Accelerator
MLC	Multileaf Collimator
MRI	Magnetic Resonance Imaging
MV	Megavoltage
MVCT	Megavoltage Computed Tomography
NTCP	Normal Tissue Complication Probability
PDD	Percent Depth Dose
PET	Positron Emission Tomography
RF	Radiofrequency
RIC	Radiation Induced Current
SNR	Signal to Noise Ratio
SPECT	Single Photon Emission Computed Tomography
SSD	Source to Surface Distance
TCP	Tumor Control Probability

1. Introduction

1.1. Historical Overview

On a Friday evening, on November 8, 1895, Professor Wilhelm Conrad Röntgen of the University of Würzburg, Germany, was the first to observe the effects of “a new kind of rays” while performing some preliminary cathode ray experiments with a Hittorf-Crookes’ vacuum tube. Eight weeks later, at the end of December 1895, the “Preliminary Communication” entitled simply “On a new kind of rays” was being published, detailing the thorough experiments with the so called X-rays, that Röntgen had done since that initial observation. Within days of this publication, Röntgen’s discovery sparked the imagination and interest of both the scientific community and the general public not only in Germany but all around the world. With shadowgraphs of hands and other body parts being made on both sides of the Atlantic according to the Röntgen method, possible medical applications of the x-rays were already being discussed [1]. Then, a few months later, in 1896, the French physicist Henry Becquerel was discovering natural radioactivity [2] and two years later in 1898 the Curies were reporting on their discovery of radium [3]. These three major discoveries led the way to a whole new era in both science and medicine. Although the effect of the newly discovered radiation on the biology of the living tissue was almost immediately apparent, the interaction mechanisms were not yet well understood. Nevertheless, the speed with which new technologies were being developed and implemented in radiation therapy was unprecedented. Less than two months after their discovery, Emil Grubbe became the first person to apply x-rays to the treatment of cancer in January 1896 in Chicago [2], and in 1899 the first cancer patient cured by radiotherapy was reported [3]. By the beginning of the 1900’s however, the first side effects of the exposure to radiation were also becoming apparent, with the first cases of radiation induced leukemia, lost fingers and skin ulcerations being reported [2].

Over the next few decades ways of producing x-rays more efficiently and of increasing their peak energy were investigated. In 1913, William Coolidge develops the 'hot-cathode tube' [2] capable of producing x-rays with a peak energy of 140 kV [4]. Within a few more years, x-rays with peak energies of 200 – 500 kV were becoming available for the so called ortho-voltage treatment of deep seated tumors. The only other source for high energy photons for more than twenty years since its discovery was radium, whether used by direct application, interstitial or body cavity insertion (also known as brachitherapy) [2], or in tele-radium units [5].

By the end of the 1940's physicists, biologists, clinicians, and radiologists had worked together, contributing immensely to the better understanding of the effects of radiation on the living tissue. Concepts like depth dose and isodose diagrams had appeared [6], the benefits of fractionated radiotherapy had been demonstrated, and correlations between radiosensitivity and oxygenation had been found [2]. Then in 1948, D.W. Fry develops the first therapy dedicated linear accelerator, making use of the microwave technology developed in England before and during World War II. The 1950's saw the rise in popularity of the high energy teletherapy units such as the ones containing the new artificially produced cobalt-60 [2]. After being developed into a treatment unit by Harold Johns and his group in Saskatoon, cobalt-60 was used to treat the first patient in 1951 in London Ontario, Canada [4]. Although cobalt-60 units have all but disappeared from clinics in the developed world, being slowly phased out by the higher energy linear accelerators (linacs), their robustness, ease of use and relatively low maintenance still makes them the unit of choice for teletherapy in many developing countries around the world [2]. In the 1960's computers were introduced in treatment planning to calculate dose distributions, at first only being used to create universal isodose distribution atlases and later on, with the help of computed tomography (CT), to create individualized dose distributions for each patient [4]. It had been recognized early on that accurate localization of the tumor and the critical surrounding structures [6], is vital to the success of radiotherapy. In the 1970's new imaging tools like CT and magnetic resonance imaging (MRI)

started being used, allowing for diagnosis and the localization of both malignant disease and the adjacent critical structures like never before [4].

With the tremendous advances in computer power, over the last twenty years, treatment methods and techniques like three dimensional conformal radiation therapy (3D-CRT), intensity modulated radiation therapy (IMRT), multileaf collimation (MLC), tomotherapy, treatment gating, adaptive radiation treatment (ART) and others [7], have become part of the daily arsenal in the fight against cancer. These treatment methods are making use of the information from multiple imaging techniques ranging from x-rays, CT, MRI, to positron emission tomography (PET), single photon emission computed tomography (SPECT), and ultrasound, to deliver highly shaped, conformal doses to tumors, allowing for an increase in the dose delivered to the primary tumor while at the same time minimizing normal tissue complications [4].

1.2. Image Guided Radiation Therapy

As stated in the previous section, all of the advances in radiation therapy over the past century have been driven by the desire to maximize the tumor control probability (TCP) by increasing the dose to the diseased area, while at the same time minimizing the normal tissue complication probability (NTCP), by sparing as much of the healthy tissue as possible. At first this was achieved by increasing the treatment energies from orthovoltage x-rays to cobalt-60 to megavoltage linacs, and more recently, by shaping the radiation field and implementing dynamic beam motion [7]. At the same time, it was realized that daily localization of malignant tissue and its alignment to radiation beam is critical to the success of advanced radiotherapy treatments. Uncertainties in the exact position and size of the tumor at any given time lead to larger treatment volumes, which in turn restrict the radiation dose that can be delivered without severe normal tissue toxicity [8]. Conventionally, the patient was set up in the treatment position with the help of surface marks. This positioning method assumed a good correlation between internal and external anatomy, which is not

always the case. The need for more certainty and precision in tumor localization and alignment with the treatment beam led to advances in imaging technology which, over the last couple of decades, paralleled the advances in radiation therapy [9].

To address the aforementioned uncertainties in tumor location, the International Commission on Radiation Units (ICRU) Report Number 50, defined three concepts which are important to treatment planning and treatment delivery. The *Gross Tumor Volume* (GTV) is defined as the gross palpable or visible extent of malignant tissue, which may consist of the primary tumor, or metastases. The *Clinical Target Volume* (CTV) is the volume around the GTV that contains subclinical or microscopic malignant tissue, which has to be eliminated for the curative or palliative therapy to be effective. The *Planning Target Volume* (PTV) is the 3D geometric margin that encompasses the CTV and accounts for day to day patient setup variations, CTV motion, or CTV size and shape changes due to internal organ motion or deformations. The PTV is the volume used for the planning and prescription of dose, and the dose distribution delivered to the PTV is considered representative of the dose delivered to the CTV [4]. These three target volumes, as defined by ICRU – 50 are schematically represented in Figure 1-1.

Image guided radiation therapy (IGRT) refers to treatment decisions made on the basis of frequent imaging of the patient in treatment position, taken during the course of a radiation therapy treatment. IGRT makes use of daily images of the patient in treatment position to better align the tumor volume with the radiation beam, thus minimizing day to day setup variations, and allowing for a reduction in the PTV and consequently a reduction in the volume of intentionally irradiated healthy tissue. Current imaging methods used by IGRT include: 2D radiographic megavoltage (MV) and kilovoltage (kV) imaging, kV fluoroscopic imaging, cone beam computed tomography (CBCT), megavoltage computed tomography (MVCT), and 3D ultrasound [9].

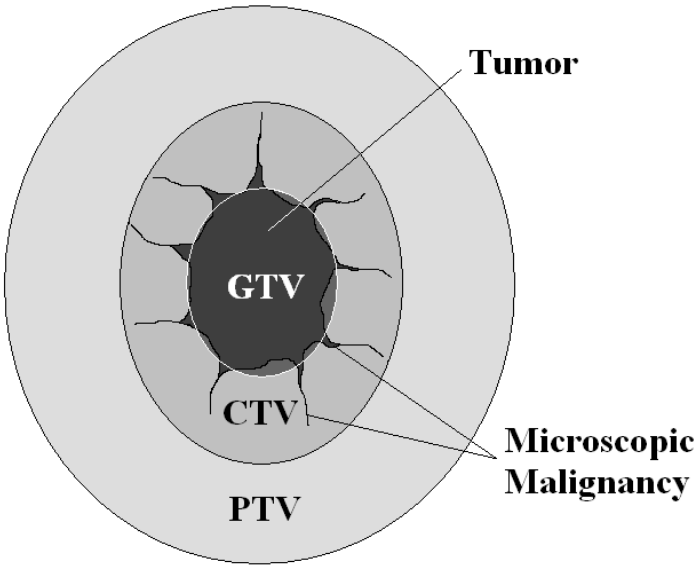

Figure 1-1: A 2-D schematic representation of the target volumes in radiotherapy according to ICRU – 50. The tumor and target volumes are all three dimensional.

The 2D radiographic MV imaging, also called an electronic portal imaging device (EPID), is obtained by using the treatment beam itself and an active matrix flat-panel imaging detector. This technique gives a beam's eye view of the patient which helps in making adjustments to the treatment position. However, due to the superposition of 3D anatomy into 2D MV radiographs and due to poor contrast between the various tissue types at MV photon energies, this method suffers from very poor soft tissue contrast, even more so compared to the conventional kV radiographs. Thus, by using the treatment beam, only the position of the bone structures and airways with respect to the treatment field can be compared with reference images. Unfortunately, many tumors can move considerably with respect to the bones from one treatment day to the next. To be able to infer the position of the actual tumor using this method, radio opaque markers have to be implanted in or near the target volume [8, 9] which requires an invasive procedure and may be plagued with side effects. Typical doses delivered to patients during the acquisition of 2D MV radiographs are between 4 and 16 cGy per image pair [10]. For this reason the modern EPIDs are mainly used to measure the modulated treatment output or the patients' exit dose which can be compared to the ones

calculated by the treatment planning system, thus providing a very good quality assurance of the treatment process [8].

Because of the limitations of MV imaging, kV images, obtained by using machine- or room-mounted kV x-ray tubes and detectors, are also being used. KV images have better contrast, and deliver a much lower dose to the patient than MV images; however, due to a 2D projection of 3D structures in kV radiographs, implanted markers still have to be used to be able to localize soft tissue structures [8, 9], and exact beam's eye view images can no longer be obtained. Also kV x-rays have been successfully used for fluoroscopic real time tracking of implanted markers during the treatment of lung tumors [11], and to asses organ motion for the thorax and upper-abdominal cavity during treatment planning [10].

The imaging methods described so far are inherently two dimensional, and at least two images have to be taken to be able to localize the structures that are surrogate to the tumour (e.g. bony landmarks and/or implanted markers) in three dimensions. Moreover, the detectable patient motions are limited to those about the axes perpendicular to the imaging plane. For a better localization of the target volume in 3D, CBCT images are obtained using a kV x-ray tube and flat panel detector mounted on the treatment unit with the same axis of rotation as the MV treatment beam [9]. A kV CBCT scan acquires 3D images with slightly better soft tissue contrast, delivering only a fraction of the dose, typically between 0.5 and 4 cGy [10], compared to MV radiographs. MV CBCT images can also be acquired using the EPID and the treatment beam. However due to the high doses needed for acquiring an MV CBCT scan (5 – 15 cGy [12]) they are mainly used for patients with orthopaedic implants that usually cause artifacts on kV scans. Although the cone beam images usually offer enough soft tissue contrast to eliminate the need for implanted markers in many body sites, they are limited to positioning the patient before treatment, as real time volumetric imaging, during treatment, is not available [8] since the data acquisition requires a concentric rotation of the source and detector assembly around the patient. Also, the soft tissue contrast in CBCT images, even at kV energies, is generally inadequate for localizing malignant tissue in pelvis, abdominal cavity, brain and extremities.

A tomotherapy unit (Tomotherapy, Madison, Wi) [13] is a treatment unit conceptually based on a CT scanner in which the kV x-ray source is replaced by a 6 MV linac, and the collimating jaws are replaced by a binary collimator. Tomotherapy delivers highly conformal IMRT in a rotational, slice by slice fashion while the patient is slowly translated through the bore [8]. This unit can acquire daily helical MVCT scans of the patient in the treatment position which are used to adjust for positioning errors, align the treatment volume, or even reconstruct the delivered dose [10]. However, tomotherapy is not really well suited for treating moving targets, due to its slice by slice mode of treatment [8], or for real time imaging since the treatment and imaging source are one and the same. Also the imaging doses typically delivered by the helical MVCT are between 1 and 3 cGy [14]. Moreover, due to the use of MV photons for imaging, the quality of CT images obtained by the MVCT is considerably poorer compared to diagnostic CT scanners.

Ultrasound is another 3D imaging modality used to visualize soft tissue before treatment, and to align the tumor with the treatment beam. However the use of ultrasound is limited to superficial or pelvic locations (usually prostate), since a good acoustic window is required. Also it can not be used during the actual radiation treatment, since usually an operator is needed [8]. Some studies have shown that ultrasound is an adequate method for guiding the treatment of prostate cancer and is simpler and more expeditious to use daily than CT [15], while other studies found that it can not safely replace the use of implanted fiducial markers for treatment guidance at the same site [16]. It has been also argued that ultrasound is too susceptible to user variability and that the pressure from the probes used for acquiring the signal can introduce shifts and displacements of the internal organs [8].

All of the imaging methods currently used by IGRT and described so far suffer from poor soft tissue contrast, lack tumor specific contrast and are currently unable to provide real time images during the radiotherapy treatment. Also, except for ultrasound, all the other imaging modalities use ionizing radiation, thus slightly increasing the patient's overall dose [8, 9]. The logical next step, that

would overcome all of the above mentioned limitations, would be to introduce MRI in IGRT. MRI can provide exquisite soft tissue contrast and tumor visualization by appropriate manipulation of the pulse sequences, has real time imaging capability during the delivery of the radiation beam, and does not use ionizing radiation. An integrated radiation treatment MRI unit would be capable of real time tumor visualisation and tracking, thus further reducing the PTV. Currently three groups around the world are actively trying to integrate a teletherapy system with an MRI imaging system: two linac-MR systems [17, 18] and a cobalt-MR system [19].

1.3. Linac-MR at the Cross Cancer Institute

Our research group at the Cross Cancer Institute in Edmonton, Alberta, proposed a Linac-MR design, which mechanically couples a bi-planar low field magnet MRI with a 6 MV linac. Currently there are two proposed design configurations, namely transverse and parallel, referring to the orientation that the central radiation beam axis has with respect to the main magnetic field. In the transverse configuration, presented in Figure 1-2, the linac is mounted on the side of the MRI magnet and the radiation field can reach the patient unobstructed at any gantry angle. Both the linac and the MRI magnet rotate together on the same gantry [17].

A small scale prototype 0.2 T permanent bi-planar magnet, attached to a refurbished 6 MV linac and mounted on a stationary gantry has been built using the transverse configuration. This prototype was used to acquire the first ever MR images during MV photon irradiation [17]. As the magnetic field is always perpendicular to the radiation beam, this geometry provides a strong interaction between the magnetic field and the secondary electrons produced in the patient. This results in unwanted dose perturbations in the patient, especially within lung, lung-tissue interfaces and other airways where the electrons can travel longer distances and change directions due to main magnetic field of the MRI [20 – 25]. This effect becomes even more significant at higher magnetic fields.

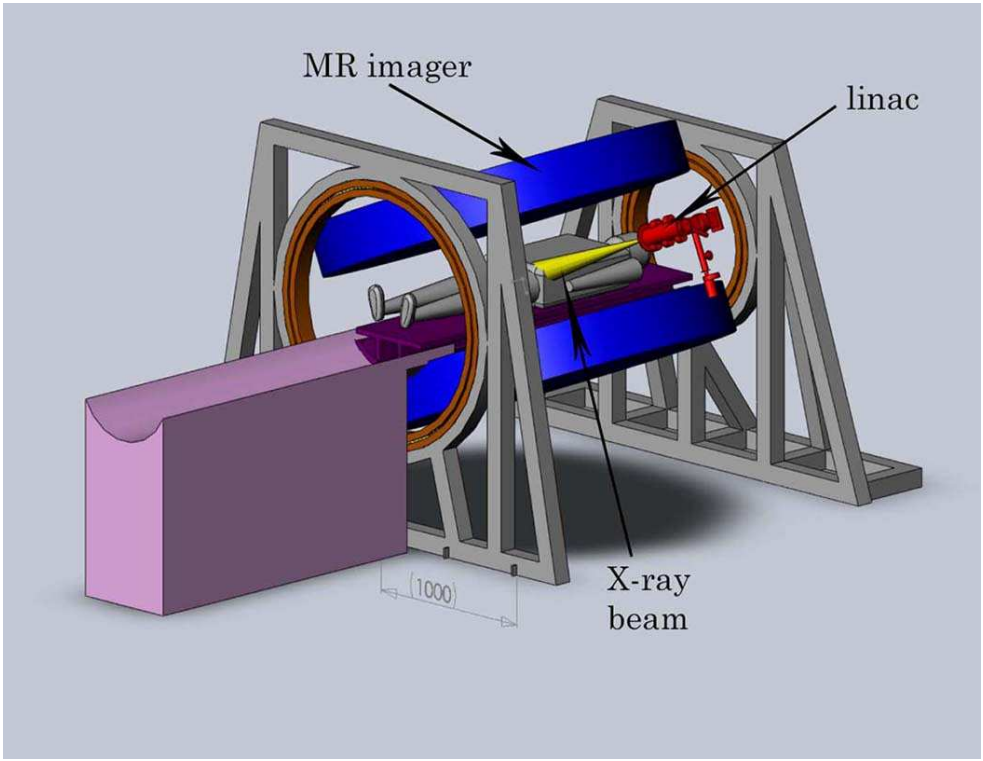

Figure 1-2: Transverse configuration of the CCI Linac-MR system. With permission of Emanuel Blosser.

The parallel configuration was designed to circumvent the ill-effects of the magnetic field on the patient dosimetry. The parallel linac-MR configuration, presented in Figure 1-3, still uses a bi-planar magnet MRI mechanically coupled with a linac however the linac is irradiating the patient through an opening in one of the poles along the magnet's axis of symmetry. Similar to the transverse configuration, the magnet and linac rotate together on the same gantry. In this geometry, the path of electrons that travel near parallel to the magnetic field of MRI is unaltered while the electrons escaping the irradiated regions may be forced back thus sharpening the treatment beam penumbra.

Our group has been investigating issues that arise when coupling a linac with an MRI, such as dosimetry considerations, and mutual interference between the two systems, and has come up with solutions [23-28] for many of them.

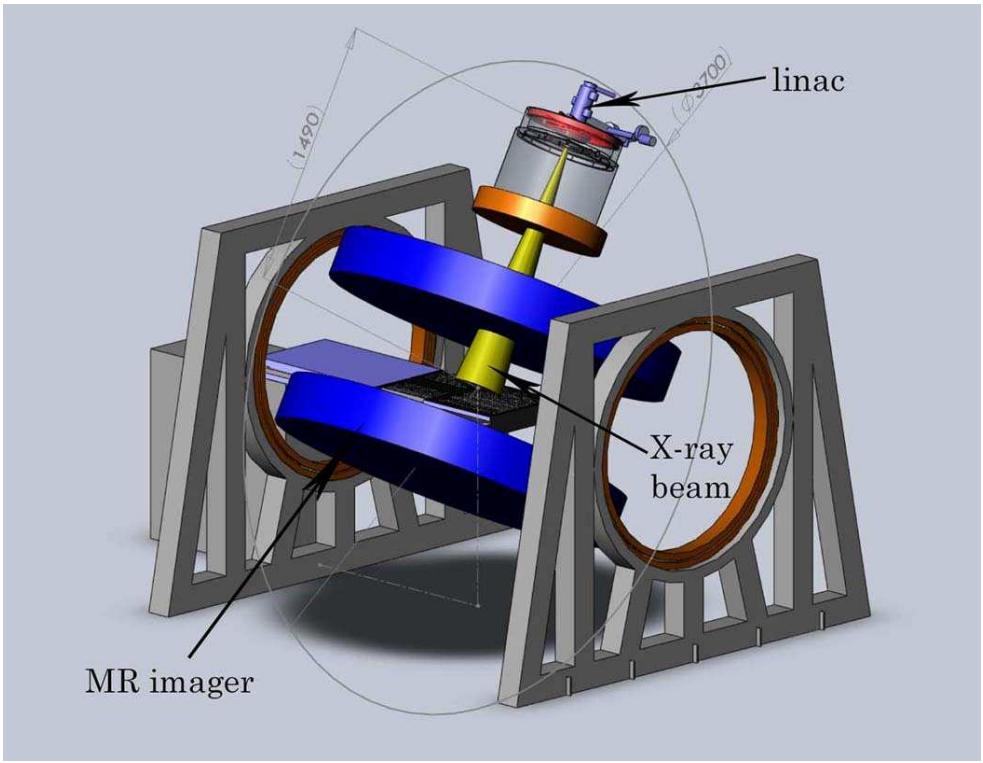

Figure 1-3: Parallel configuration of the CCI Linac-MR system. With permission of Emanuel Blosser.

1.4. Motivation and Outline

MRI uses radio frequency (RF) coils to both excite proton magnetizations and to receive the signal from their precessing magnetic moments. During a real time treatment imaging session with one of these integrated units, whether the transverse or the parallel configuration is used, the RF coils will be exposed to the linac's direct pulsed irradiation. This causes a measurable current to be induced in the coil [27] that can potentially degrade the acquired MRI image. For real time tumour tracking to be feasible, each acquired image must be spatially accurate and must have an adequate signal to noise ratio (SNR), thus any potential causes for reduction of the SNR must be studied and eliminated or at least reduced. The work presented in this thesis, experimentally investigates methods of removing or significantly reducing any currents induced in the RF coil conductor due to the pulsed irradiation, as well as the effects that RF coil materials, present in the

treatment beam, have on the skin dose. It is assumed that the active components such as receive/transmit switch and pre-amplifier are physically separated from the RF coil structure and therefore are placed outside the radiation beam area. Thus, the evaluation of the effect of irradiating these components is outside the scope of this thesis. In the following, the chapter by chapter outline of this thesis will be presented.

In Chapter 2 the theory pertaining to this work is introduced. It starts with discussing the ways high energy photons can interact with matter, with an emphasis on photoelectric effect, Compton scattering and pair/triplet production. The exponential attenuation of a photon beam as it enters a material is then presented. Some quantities describing the radiation beam and energy transfer are then introduced leading to defining and explaining the differences between kerma and dose. Electronic equilibrium is defined and an explanation of how the lack of it can lead to radiation induced currents is then offered. Due to the nature of some materials used during the work presented in this thesis, electrets are defined next and some of their properties as well as how they behave when under high energy photon irradiation are briefly explained.

In Chapter 3 the materials and methods used for the various experiments performed, are described and explained. A general description of the simplified experimental setup used for measuring and reducing the radiation induced conductivity in thin conductors is first offered. Then a brief description of the equipment is presented. The detailed descriptions of individual setups and methods used to reduce or remove the induced current are given next. For the investigation into how placing an RF coil in the treatment beam would affect the surface dose, the measurement setup, and the various coil materials are presented. The chapter concludes with the description of the setup used to record the radiation induced current in an RF coil, both with and without a magnetic field present.

Chapter 4 presents the results of all the experiments described in Chapter 3. Some preliminary results that lead to some setup adjustments are first presented. The reduction of radiation induced current in thin conductors and

factors that influence the measurements are shown next, leading into the reduction of the induced current in an aluminum surface coil built in house. The surface dose measurements taken with various distances between the solid water phantom and the coil materials are then described, and the recorded RF coil induced current traces with and without a magnetic field present conclude the chapter.

Chapter 5 presents a brief discussion of these results, and Chapter 6 offers a short conclusion for all the work presented in this thesis and suggests future possible investigations.

References:

1. O. Glasser, *Wilhelm Conrad Rontgen and The Early History of the Roentgen Rays*, Charles C Thomas, Springfield Illinois, pp 1 – 28, 1934.
2. J. Bernier, E.J. Hall, and A. Giaccia, *Radiation oncology: a century of achievements*, Nature Reviews Cancer **4**, 737 – 747, 2004.
3. C.A. Perez, L.W. Brady, J.L. Roti "Overview" *Principles and Practice of Radiation Oncology 3rd Edition*, Editors: C.A. Perez and L.W. Brady, Philadelphia, PA: Lippincott-Raven, pp.1 – 78, 1998.
4. J. Van Dyk *The Modern Technology of Radiation Oncology*, Editor: J. Van Dyk, Medical Physics Publishing, Madison, Wisconsin, pp. 1- 18, 1999.
5. E. Lysholm, *Apparatus for the production of a narrow beam of rays in treatment by radium at a distance*, Acta Radiologica, **2**, 516 – 519, 1923
6. G. Failla, *An objective method for the administration of x-rays*, Acta Radiologica, **4,** 85 – 128, 1925.
7. J. Van Dyk *The Modern Technology of Radiation Oncology, Volume 2*, Editor: J. Van Dyk, Medical Physics Publishing, Madison, Wisconsin, pp. 1- 29, 2005.
8. D. Verellen, M. De Ridder, N. Linthout, K. Tournel, G. Soete, G. Storme *Innovations in image-guided radiotherapy*, Nature Reviews. Cancer **7,** 949 – 960, 2007.
9. L.A. Dawson and D.A. Jaffray *Advances in Image-Guided Radiation Therapy*, Journal of Clinical Oncology **25(8)** 938-946, 2007.
10. L.A. Dawson, M.B. Sharpe *Image-guided radiotherapy: rationale, benefits, and limitations*, Lancet Oncol., **7**, 848-858, 2006.

11. H. Shirato, S. Shimizu, K. Kitamura, T. Nishioka, K. Kagei, S. Hashimoto, H. Aoyama, T. Kunieda, N. Shinohara, H. Dosaka-Akita, and K. Miyasaka, *Four-dimensional treatment planning and fluoroscopic real-time tumor tracking radiotherapy for moving tumor*, Int. J. Radiation Oncology Biol. Phys., **48**, 435-442, 2000.

12. J. Pouliot, A. Bani–Hashemi, J. Chen, et al. *Low-dose megavoltage cone-beam CT for radiation therapy*. Int J Radiat Oncol Biol Phys.;61(2):552–560, 2005.

13. T. R. Mackie, T. Holmes, S. Swerdloff, P. Reckwerdt, J. O. Deasy, J. Yang, B. Paliwal, and T. Kinsella, *Tomotherapy - a new concept for the delivery of dynamic conformal radiotherapy*, Medical Physics, **20**, 1709-1719, 1993.

14. A.P. Shah, K.M. Langen, K.J. Ruchala, A. Cox, P.A. Kupelian, and S.L. Meeks *Patient Dose from Megavoltage Computed Tomography Imaging*, Int. J. Radiation Oncology Biol. Phys., **70 (5)**, 1579–1587, 2008

15. J. Lattanzi, S. McNeeley, W. Pinover, E. Horwitz, I. Das, T.E. Schultheiss, and G.E. Hanks, *A comparison of daily CT localization to a daily ultrasound-based system in prostate cancer*. Int. J. Radiat. Oncol. Biol. Phys. **43**, 719–725, 1999.

16. H. Johnston, M. Hilts, W. Beckham, E. Berthelet, *3D ultrasound for prostate localization in radiation therapy: A comparisonwith implanted fiducial markers*, Medical Physics, **35 (6)**, 2403 – 2413, 2008.

17. B. G. Fallone, B. Murray, S. Rathee, T. Stanescu, S. Steciw, S. Vidakovic, E. Blosser, and D. Tymofichuk, *First MR images obtained during megavoltage photon irradiation from a prototype integrated linac-MR system*, Medical Physics, **36**, 2084-2088, 2009.

18. B. W. Raaymakers, J. J. W. Lagendijk, J. Overweg, J. G. M. Kok, A. J. E. Raaijmakers, E. M. Kerkhof, R. W. van der Put, I. Meijsing, S. P. M. Crijns, F. Benedosso, M. van Vulpen, C. H. W. de Graaff, J. Allen, and K. J. Brown, *Integrating a 1.5 T MRI scanner with a 6 MV accelerator: proof of concept*, Phys. Med. Biol., **54**, N229-N237, 2009.

19. J. F. Dempsey, D. Benoit, J. R. Fitzsimmons, A. Haghighat, J. G. Li, D. A. Low, S. Mutic, J. R. Palta, H. E. Romeijn, and G. E. Sjoden, *A Device for Realtime 3D Image-Guided IMRT,* Int. J. Radiat. Biol., **63**, S202-S202, 2005.

20. A. J. E. Raaijmakers, B. W. Raaymakers, and J. J. W. Lagendijk, *Experimental verification of magnetic field dose effects for the MRI-accelerator*, Phys. Med. Biol., **52**, 4283-4291, 2007.

21. A. J. E. Raaijmakers, B. W. Raaymakers, and J. J. W. Lagendijk, *Magnetic-field-induced dose effects in MR-guided radiotherapy systems: dependence on the magnetic field strength*, Phys. Med. Biol., **53**, 909-923, 2008.

22. A. J. E. Raaijmakers, B. W. Raaymakers, S. van der Meer, and J. J. W. Lagendijk, *Integrating a MRI scanner with a 6 MV radiotherapy accelerator: impact of the surface orientation on the entrance and exit dose due to thetransverse magnetic field*, Phys. Med. Biol., **52**, 929-939, 2007.

23. C. Kirkby, B. Murray, S. Rathee, and B. G. Fallone, *Lung dosimetry in a linac-MRI radiotherapy unit with a longitudinal magnetic field*, Med. Phys., **37**, 4722-4732, 2010.

24. C. Kirkby, T. Stanescu, S. Rathee, M. Carlone, B. Murray, and B. G. Fallone, *Patient dosimetry for hybrid MRI-radiotherapy systems*, Med. Phys., **35**, 1019- 1027, 2008.

25. C. Kirkby, T. Stanescu, and B. G. Fallone, *Magnetic field effects on the energy deposition spectra of MV photon radiation*, Phys. Med. Biol., **54**, 243-257, 2009.

26. B. Burke, M. Lamey, S. Rathee, B. Murray, and B. G. Fallone, *Radio frequency noise from clinical linear accelerators*, Phys. Med. Biol., **54**, 2483- 2492, 2009.

27. B. Burke, B. G. Fallone, and S. Rathee, *Radiation induced currents in MRI RF coils: application to linac/MRI integration*, Phys. Med. Biol., **55**, 735-746, 2010.

28. M. Lamey, B. Burke, E. Blosser, S. Rathee, N. De Zanche, and B. G. Fallone, *Radio frequency shielding for a linac-MRI system*, Phys. Med. Biol., **55**, 995- 1006, 2010.

2. Theory

Since this thesis is mainly concerned with the interaction of a pulsed photon beam with the materials found in the RF coils of the MRI, a brief overview of the various modes of photon interaction with matter is in order. The instantaneous effect of pulsed radiation in RF coils is the creation of charge imbalance in the thin conductor of the coil winding. Thus, the following overview emphasizes the types of photon interactions in which the electrons within the matter gain sufficient energy and can travel farther away from the point of energy transfer. In the case of a thin conductor, the energetic electrons have a finite probability of leaving the conductor altogether, thus, creating the above mentioned charge imbalance. The charge imbalance creates an undesired current which can be removed by replacing the electrons leaving the conductor. In the case of a dielectric, like the Teflon used during this work, the energetic electrons cause charge deposition and polarization. In the last section of this chapter some properties of the special class of dielectrics that Teflon is a part of are described.

2.1. Interactions of High Energy Photons with Matter

High energy photons interact with different materials in various ways depending on the photon's energy $h\nu$ and the material's atomic number Z. The types of photon interactions that are usually considered in radiological physics are: Rayleigh (or coherent) scattering, the photoelectric effect, Compton (or incoherent) scattering, pair and triplet production, and photonuclear interactions. The most important of these are the middle three, since they result in the transfer of energy to matter indirectly, by ionizing atoms and setting electrons in motion. Figure 2-1 shows the regions of Z and $h\nu$ in which each of the photoelectric, Compton, and pair production interactions dominate. Each of the above mentioned interactions will be discussed, with emphasis on the main three [1] and with particular emphasis on the Compton interaction, since, as seen from Figure

2-1, it is the dominant interaction for most materials in the radio-therapeutic energy range (~1 to 10 MeV).

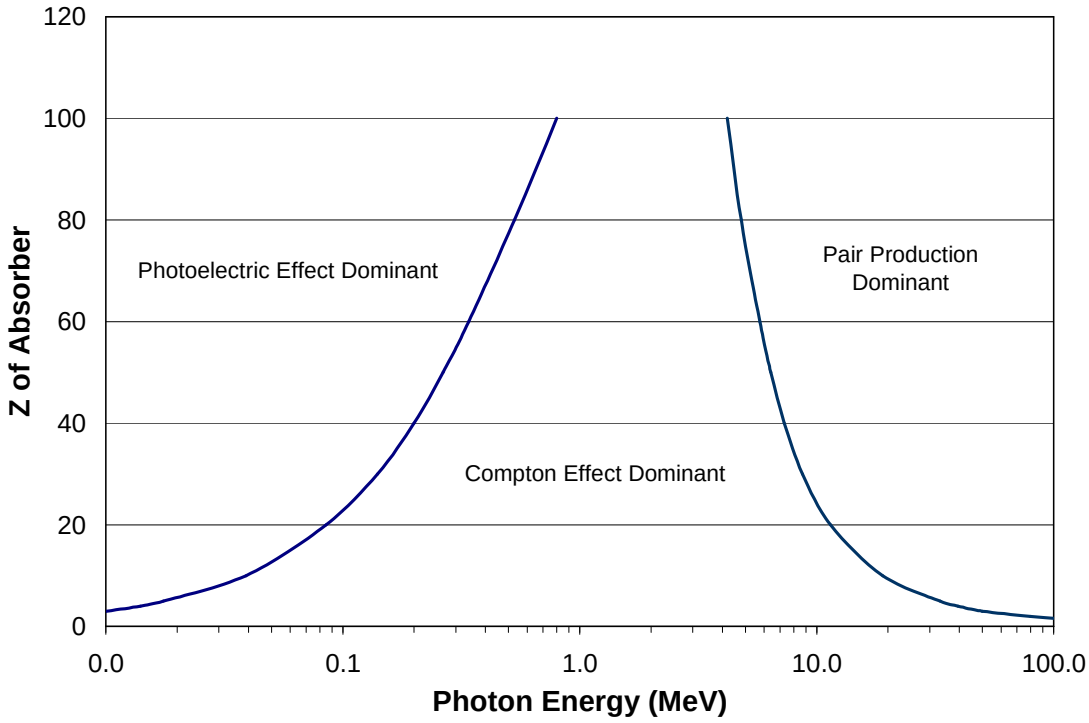

Figure 2-1: Relative importance of the three major types of high energy photon interactions. The curves show the atomic numbers and photon energies for which the adjacent interactions have about the same probability of happening. (Data taken from NIST [2]).

2.1.1 Coherent Scattering

When a high energy photon passes over an atom, the photon's associated electric field will set the electrons in the atom into momentary vibration. The oscillating electrons will emit radiation of the same wavelength as the incident photon. These electromagnetic waves from the electrons within the atom combine with each other, forming the scattered wave. This process is called coherent scattering. None of the incident photon's energy is transferred to kinetic energy in this process. The probability (also called cross section) of coherent scattering, usually denoted by σ_{coh}, decreases rapidly with increasing photon energy and with decreasing atomic number [1, 3] and is of little importance in the radiotherapy energy range for most materials.

2.1.2 Photoelectric Effect

In the photoelectric process, illustrated schematically in Figure 2-2, a bound electron is ejected from the K, L, M, or N shells, following a collision of an energetic photon with an atom.

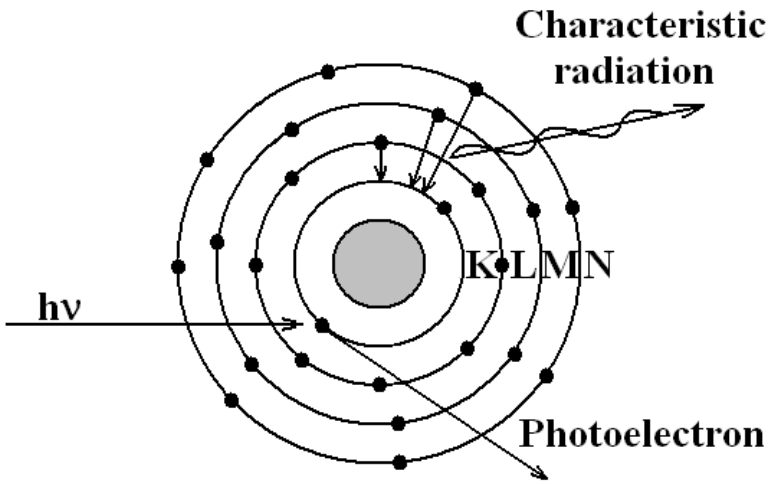

Figure 2-2: Schematic representation of the interaction of a photon with an atom resulting in the ejection of a photoelectron from the K shell.

The photon is absorbed and ceases to exist, and the ejected electron, also called a photoelectron, leaves the atom with a kinetic energy $h\nu - E_B$, where E_B is the electron's binding energy. The atom, which is temporarily left in an excited state, returns to the ground state by emission of characteristic x-ray radiation and Auger electrons. The characteristic x-ray is emitted when the vacancy left by the photoelectron is filled by an electron falling from a less tightly bound shell. Any part of the binding energy that is not removed by a characteristic x-ray is disposed of by means of the Auger effect. In the Auger process, an atom with excess energy ejects one or more of it's electrons with enough kinetic energy to collectively account for the excess. The probability that an electron will get ejected from the atom through the photoelectric process is greatest when the incident photon has just enough energy to remove the electron from its shell [1, 3]. The photoelectric cross section (τ) decreases with increasing energy and with decreasing atomic number. With increasing photon energy, the probability

that a photoelectric interaction will take place decreases rapidly, approximately like $1/(h\nu)^3$. For high atomic number materials the cross section per atom varies roughly as Z^4, while for low atomic number materials it varies like $Z^{4.8}$ [3]. For the materials used during the present work, the photoelectric effect was the dominant interaction for photons with energies of up to about 150 keV. Thus, although setting electrons in motion, potentially with sufficient energy, the photoelectric effect is not the main interaction responsible for the charge depletion in the conductor of a RF coil irradiated with a photon beam in the radio-therapeutic energy range.

2.1.3 Compton Scattering

In the Compton scattering process, illustrated in Figure 2-3, a high energy photon interacts with a loosely bound electron. Part of the photon's energy hν, is imparted to the electron which is set in motion with a certain energy E at an angle ϕ, while the rest of the energy is carried away by a photon of energy hν', at an angle θ.

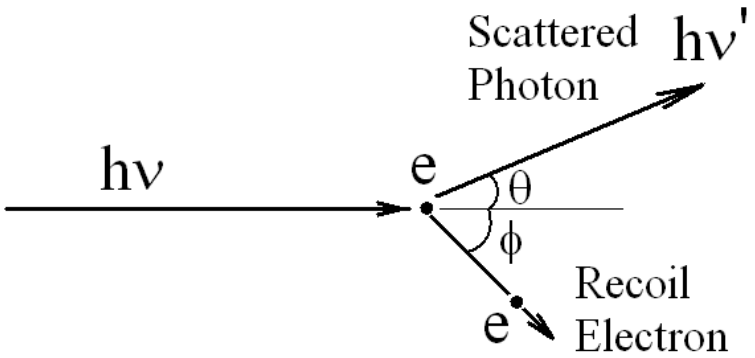

Figure 2-3: Schematic representation of the Compton scattering process.

By using conservation of energy and momentum, and with the help of Figure 2-3, the energy carried away by the scattered photon in a Compton collision can be shown to be:

$$h\nu' = h\nu \cdot \frac{1}{1+\alpha(1-\cos\theta)} \qquad (2\text{-}1)$$

While the energy of the scattered electron is:

$$E = h\nu - h\nu' = h\nu \cdot \frac{\alpha(1-\cos\theta)}{1+\alpha(1-\cos\theta)} \tag{2-2}$$

Where, in both cases, α is the ratio of the incident photon energy to the electron rest energy:

$$\alpha = \frac{h\nu}{m_0 c^2} \tag{2-3}$$

Where m_0 is the electron's rest mass and *c* is the speed of light in vacuum.

From the above equations, two extreme cases are immediately apparent. In the first case, the scattered photon angle could be θ = 180°, meaning the photon has made a direct collision with the electron and is being scattered straight back while the electron is travelling straight forward (ϕ=0°). In this case, the electron acquires the maximum energy leaving the scattered photon with minimum energy.

$$E_{\max} = h\nu \cdot \frac{2\alpha}{1+2\alpha} \tag{2-4}$$

$$h\nu'_{\min} = h\nu \cdot \frac{1}{1+2\alpha} \tag{2-5}$$

In the second extreme case, the scattered photon could essentially go straight forward with $\theta \approx 0$ and the electron emerge at a right angle ϕ=90°, meaning the photon has made a grazing hit with the electron and transferred virtually no energy to it, as substituting $\cos\theta = 1$ into Equations (2-1) and 2-2 gives $E = 0$ and $h\nu' = h\nu$. Between these two cases all the intermediate photon and electron scattering angles, and a spectrum of energies are possible [1, 3].

The relative probability of a Compton interaction with a free electron was determined by Klein and Nishina with the help of quantum mechanics. According

to their calculations the differential cross section ($d\sigma$) per unit solid angle ($d\Omega$) is given by:

$$\frac{d\sigma}{d\Omega} = \frac{r_0^{\,2}}{2}\left(1+\cos^2\theta\right)\cdot F_{KN} \tag{2-6}$$

Where r_0 is the so called classical electron radius given by:

$$r_0 = \frac{k\cdot e^2}{m_0 c^2} = 2.81794\times 10^{-15} m \tag{2-7}$$

With k being a constant, e the electron charge ($e = 1.6022\times 10^{-19}\ C$), and the factor F_{KN} being defined by:

$$F_{KN} = \left\{\frac{1}{1+\alpha(1-\cos\theta)}\right\}^2\left\{1+\frac{\alpha^2(1-\cos\theta)^2}{[1+\alpha(1-\cos\theta)](1+\cos^2\theta)}\right\} \tag{2-8}$$

The angle θ is the photon's scattering angle as seen from Figure 2-3, and α is as given by Equation 2-3. Multiplying Equation 2-6 by $d\Omega = 2\pi\sin\theta\, d\theta$ and integrating over all the values of θ the total probability that a photon will interact by the Compton (incoherent scattering) process is obtained, and is given by:

$$\sigma_{inc} = 2\pi\, r_0^2\left\{\left(\frac{1+\alpha}{\alpha^2}\right)\left[\frac{2(1+\alpha)}{1+2\alpha}-\frac{\ln(1+2\alpha)}{\alpha}\right]+\frac{\ln(1+2\alpha)}{2\alpha}-\frac{1+3\alpha}{(1+2\alpha)^2}\right\} \tag{2-9}$$

In Equation 2-9, σ_{inc} is independent of the atomic number Z since the electron set in motion was considered to be free for the derivation. This overestimates the probability of a Compton interaction happening, leading to substantial errors for photon energies below about 10 keV that can only be corrected by taking the electron's binding energy into account. Overall this error turns out to be small

since for photon energies below 10 keV the photoelectric effect is far more important than Compton scattering. The probability for a Compton interaction taking place decreases slowly with increasing energy [3], but for the radiotherapy energy spectrum and for the RF coil materials used for the experiments presented in this thesis, it is the dominant type of interaction.

2.1.4 Pair and Triplet Production

Pair production is the process in which a photon disappears, when passing through a Coulomb force field, usually the field near an atomic nucleus, and gives rise to an electron and a positron. This process can also take place, in the Coulomb field of an atomic electron, however, with lesser probability. The atomic electron that provides the Coulomb field also acquires substantial kinetic energy, thus two electrons and a positron are leaving the interaction site. For this reason this latter process is called *triplet production*. For pair production to occur in the nuclear field the photon is required to have a minimum energy of $2m_0c^2 = 1.022MeV$ (i.e. twice the electron rest energy).

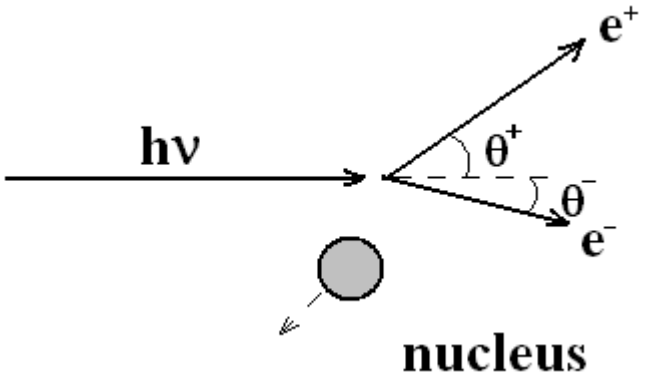

Figure 2-4: Schematic representation of the pair production process in the Coulomb field of a nucleus.

Any energy in excess of *1.022 MeV* that the photon might have is shared between the electron and the positron so that:

$$h\nu - 2m_0c^2 = E_- + E_+ \qquad (2\text{-}10)$$

Where E_- and E_+ represent the kinetic energies of the electron and the positron respectively. The total energy given to the charged particles $(E_- + E_+)$ can be divided between the electron and the positron in different ways. One of the particles might emerge having most of this total energy and the other almost none or both particles may emerge with equal energies, or they can have any distribution of energies between these two extremes [1, 3].

The cross section of pair production (κ) per unit mass is proportional to the atomic number Z. The probability increases rapidly with increasing energy above the 1.022 MeV threshold [3]. Pair and triplet production become the dominant interactions for photon energies of about 10 MeV and above, for the RF coil materials used (copper, aluminum, and Teflon). This is higher than the 6 MeV peak energy used during the experiments presented in this thesis, thus pair and triplet production play a minor role in the photon interactions responsible for the electron depletion appearing in the RF coil conductor.

2.1.5 Photonuclear Interactions

In a photonuclear interaction the nucleus of an atom is excited by an energetic photon (energy in excess of a few MeV), and emits a proton or a neutron. Protons emitted as a result of photonuclear interactions, although directly contributing to ionizations and excitations in the medium are commonly neglected, due to their low relative contribution to the overall dose compared to the other types of interactions. For clinical x-ray generators (linacs, betatrons or microtrons) that accelerate electrons to energies of 10 MeV or above, this type of interaction is responsible for the slight contamination of the x-ray beam with neutrons. This fact has to be taken into account when designing shielding, or when servicing x-ray generator parts that could get activated by these neutrons and become radioactive [1]. For the photon energies used during the present work (i.e. 6 MeV peak energy) this type of interaction has a very low probability of occurring.

2.2. Exponential Attenuation of a Photon Beam

When a high energy photon beam impinges on a material, the photons penetrate the material, and start interacting with its atoms in all the various ways described in Section 2.1. When a photon interacts, whether its path is deflected or whether it is completely absorbed and ceases to exist, it is taken out of the beam. Thus if the photon beam containing a number of N photons is passing through a thin layer Δx of an absorber, the beam will be attenuated, and have fewer photons when it emerges from the absorber. The change in the number of photons in the beam (ΔN) will be proportional to the initial number of photons (N), since the more photons in the beam, the higher the chance of them interacting. ΔN is also proportional to the thickness of the absorber (Δx) since the thicker the absorber, the greater the number of atoms in the beam's path and again the higher the probability of interaction. This can be written as:

$$\Delta N = -\mu \cdot N \cdot \Delta x \qquad (2\text{-}11)$$

In the above equation, the negative sign simply indicates that the number of photons in the beam is decreasing. Also, μ is the proportionality constant called the *linear attenuation coefficient* which represents the fraction of photons interacting in Δx divided by Δx. The *mass attenuation coefficient* (μ/ρ) is used more frequently however since unlike μ it does not depend on the density of the irradiated material; it is obtained by simply dividing the linear attenuation coefficient by the density of the attenuating medium and is measured in cm^2/g or m^2/kg. Equation 2-11 is strictly correct however only if the number of photons N remains essentially unchanged as the beam travels through the absorber. This implies that ΔN is very small compared to N and that the thin layer of absorber is infinitesimally small, such that $\mu \cdot \Delta x << 1$. If both Δx and ΔN are infinitesimal, Equation 2-11 can be rewritten in differential form:

$$dN = -\mu \cdot N \cdot dx \tag{2-12}$$

After separating the variables in Equation 2-12, integrating and solving for the constant of integration, the law of exponential attenuation is obtained:

$$N = N_0 \, e^{-\mu x} \tag{2-13}$$

Equation 2-13 gives the number of photons left in a beam which initially had N_0 photons, after it has passed through any thickness x of an absorber [3].

As a typical beam of photons interacts with matter all of the photon interactions described in the previous section may occur with various probabilities, depending on the spectrum of energies present in the beam, and on the atomic number of the irradiated material. Thus for a high energy photon beam the total attenuation coefficient (μ_{tot}), is going to be the sum of the four interaction coefficients (ignoring photonuclear interactions):

$$\mu_{tot} = \sigma_{coh} + \tau + \sigma_{inc} + \kappa \tag{2-14}$$

Where σ_{coh}, τ, σ_{inc}, *and* κ are the attenuation coefficients for coherent scattering, photoelectric effect, Compton or incoherent scattering, and pair production respectively [3]. This is illustrated in Figure 2-5, where the total mass attenuation coefficient, as well as the mass attenuation coefficient for each type of interaction (obtained by dividing each coefficient in Equation 2-14 by the density) is plotted as a function of photon energy on a log/log scale for copper. Copper was chosen since it is the conductor used in most MRI RF coils.

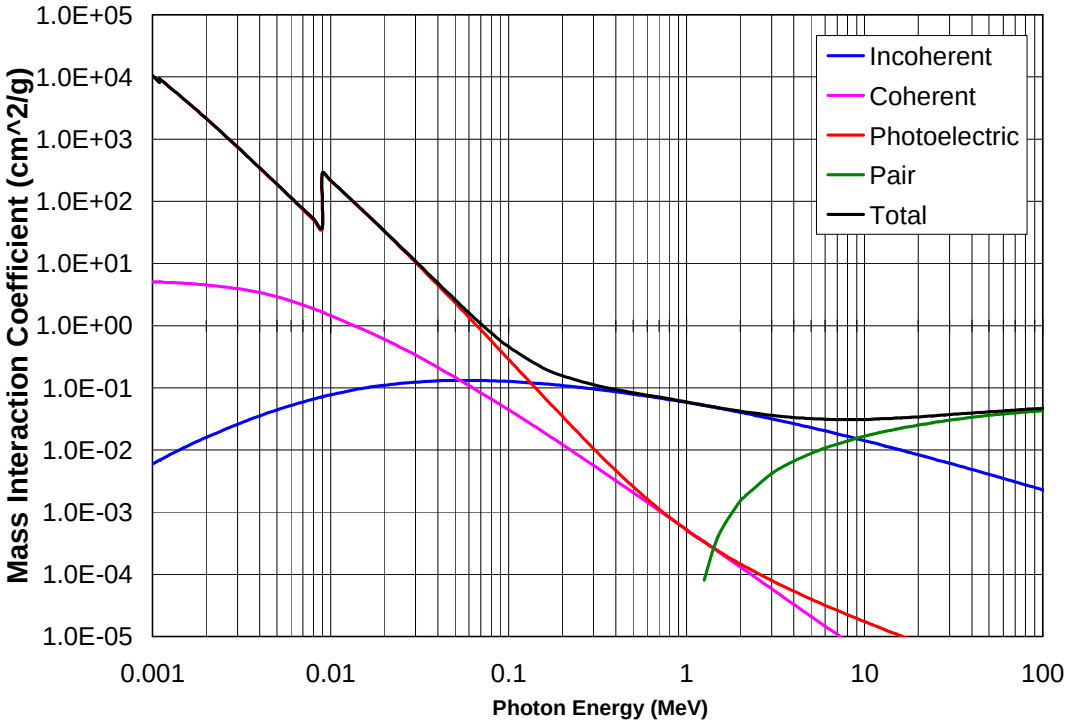

Figure 2-5: Mass attenuation coefficients for each type of interaction, and the total mass attenuation coefficient for copper as a function of photon energy on a log/log plot. (Data taken from NIST [2]).

2.3. Describing the Radiation Beam and Energy Transfer

When measuring radiation and its effects, there are two different considerations that have to be taken into account. Firstly, the amount of radiation in the beam itself has to be described, and secondly the amount of energy the beam deposits in the irradiated medium has to be quantified [3]. Both of these aspects are discussed below and some useful quantities are introduced and defined.

2.3.1. Quantities Describing the Radiation Beam

A mono-energetic photon beam can be described by the number of photons, *dN*, crossing an area, *da*, whose normal points to the direction of the

beam. The ratio of *dN* to *da* is called *fluence*, or *photon fluence*, is represented by the symbol Φ, and is expressed in units of m^{-2} or cm^{-2}.

$$Fluence; \Phi = \frac{dN}{da} \tag{2-15}$$

The *energy fluence*, represented by the symbol Ψ, describes the amount of energy crossing the area *da*, and it is expressed in units of J m^{-2} or erg cm^{-2}.

$$Energy\ Fluence; \Psi = \frac{dN \cdot h\nu}{da} \tag{2-16}$$

The *fluence rate*, ϕ, is the number of photons that pass through unit area per unit time, and it is expressed in units of $m^{-2}s^{-1}$ or $cm^{-2}s^{-1}$.

$$Fluence\ Rate; \phi = \frac{d\Phi}{dt} = \frac{d}{dt}\left(\frac{dN}{da}\right) \tag{2-17}$$

The *energy fluence rate*, ψ. represents the energy crossing a unit area per unit time. It is also called energy flux density or intensity and expressed in units of J $m^{-2}s^{-1}$ or erg $cm^{-2}s^{-1}$.

$$Energy\ Fluence\ Rate; \psi = \frac{d\Psi}{dt} = \frac{d}{dt}\left(\frac{dN \cdot h\nu}{da}\right) \tag{2-18}$$

However the tele-therapy photon beams are produced by slowing down energetic electrons within a high density target, and thus contain photons with a continuum of energy up to the maximum energy of electrons. Therefore, in order to be able to describe a realistic photon beam using the above defined quantities, one would need to know exactly the number of photons in the beam with a given energy as well as all the energies present. This requires the introduction of terms

such as spectrum (fluence differential in energy) and energy spectrum (energy fluence differential in energy) [1, 3].

2.3.2. Quantities Describing the Energy Transferred

As inferred in Section 2.1, the interaction of high energy photons with matter is a two step process. During the first step, part or all of the energy of the photon is transferred to the charged particles (usually electrons) in the irradiated medium through a series of interactions. During the second step, the energetic charged particles (also called secondary electrons) transfer this energy to the medium in a series of excitations and ionizations. To describe the first step of this interaction the quantity called *kerma* (Kinetic Energy Released per unit Mass of the medium) was introduced by the ICRU (International Commission on Radiation Units and Measurements). *Kerma* is defined in terms of the energy transferred (E_{tr}), as follows:

$$Kerma;\ K = \frac{d\overline{E_{tr}}}{dm} \tag{2-19}$$

where $d\overline{E}_{tr}$ is the mean energy transferred from the photon beam to the electrons within a volume element *dV* with mass *dm*. *Kerma* is usually expressed in units of J kg^{-1}, and it most directly relates the quantities describing the radiation beam to its effects. For instance, for a mono-energetic photon beam of energy $h\nu$ and fluence Φ the *kerma* can be written as:

$$K = \Phi \cdot \left(\frac{\mu}{\rho}\right) \cdot \overline{E}_{tr} \tag{2-20}$$

where (μ/ρ) is the mass attenuation coefficient for the medium, and $\overline{E}_{tr}$ is the average amount of energy transferred by the photons to the electrons of the medium per interaction. For a photon beam with a spectrum of energies, and a

fluence spectrum differential in energy $d\Phi(h\nu)/d\ h\nu$, the *kerma* is the sum of *kermas* from all the photons in the spectrum as shown below:

$$K = \int_0^{h\nu_{\max}} \frac{d\Phi(h\nu)}{d\ h\nu} \cdot \left(\frac{\mu(h\nu)}{\rho} \right) \cdot \overline{E_{tr}}(h\nu) \cdot d\ h\nu \tag{2-21}$$

Kerma accounts for all of the energy transferred from the photon beam to the volume of interest, whether it is retained in that volume, or escapes in the form of radiative losses or in the form of a net number of charged particles that take kinetic energy out of the volume. Radiative losses are defined as the conversion of charged particle kinetic energy into photon energy, which can escape the volume of interest or even the medium. This conversion can come about either through positron annihilation, or through the production of bremsstrahlung (or "breaking radiation") x-rays in the Coulomb field of the atom [1]. For this reason, *kerma* can be thought of as having two components: the *collision kerma* (K_c) that accounts for the kinetic energy spent by the charged particles in excitations and ionizations, and the *radiative kerma* (K_r) that accounts for the kinetic energy that is carried away by photons [1]:

$$K = K_c + K_r \tag{2-22}$$

Although *kerma* can be calculated by knowing the parameters in Equation 2-21, its experimental measurement is rather difficult [3].

The quantity that can readily be measured is the *absorbed dose* and is defined as:

$$Absorbed\ Dose;\ D = \frac{d\overline{E}_{ab}}{dm} \tag{2-23}$$

Where $d\overline{E}_{ab}$ represents the mean energy absorbed by a mass *dm* of matter. Though *dm* should be considered small enough such that the absorbed dose can be

defined at a point, it should not be too small such that the statistical fluctuations in energy deposition are significant. Although the units of *absorbed dose* are identical to the ones of *kerma*, the *absorbed dose* unit has a special name, the gray (Gy), which is defined as 1 Gy = 1 J/kg [3].

Unlike *kerma* the *absorbed dose* only accounts for the energy that is retained and remains inside the volume of interest. The absorbed dose is the most important quantity in radiation physics, since although radiation effects have either a direct or more complicated dependence on dose, it is certain that there are no effects whatsoever if $D = 0$ [1]. Also of note is the fact that *kerma* and *absorbed dose* do not take place at the same location. *Kerma* takes place at the location where a photon has set a charged particle in motion with a certain kinetic energy, while the *absorbed dose* will take place further along the track of that charged particle as it looses its kinetic energy [3].

2.4. Electronic or Charged Particle Equilibrium

Charged particle equilibrium (CPE) exists in a certain volume V if for every type of charged particle that is leaving the volume with a given energy, there is another charged particle of the same type and energy entering V [1, 4]. Although not strictly equivalent, CPE is also called *electronic equilibrium*, for although other charged particles are involved, the dominant role in radiotherapy photon beams is played by the secondary electrons [4]. Figure 2-6 (b) is an approximate schematic representation of a high energy, mono-energetic photon beam incident on a homogeneous medium. As the photons enter the material, divided into sections labeled A to H, they start interacting in all the various ways described in Section 2.1, setting electrons (represented by the straight arrows) with a range *R* in motion. Each one of the symbols (*, \, /, or |) present on the arrows in Figure 2-6 (b) represents an excitation or ionization through which the secondary electrons deposit part of their energy all the way to the end of their range *R*.

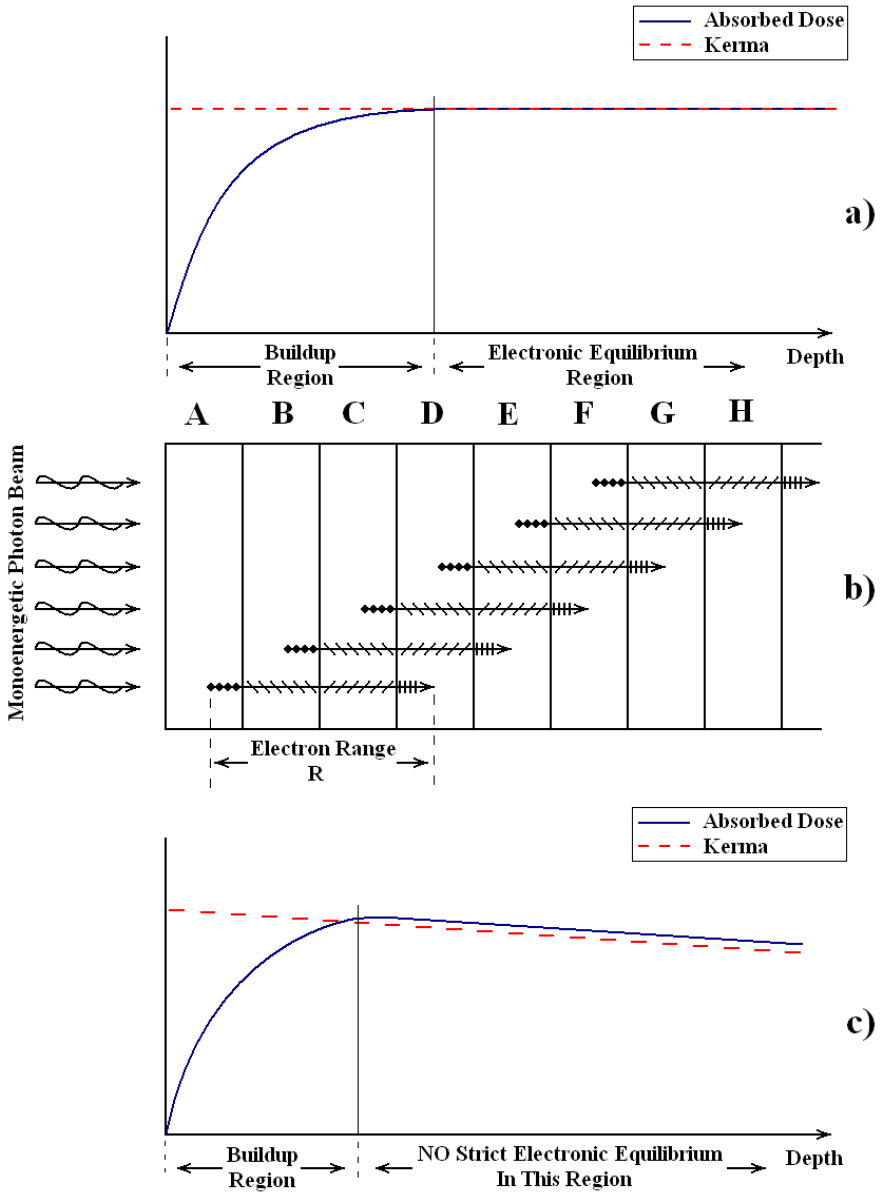

Figure 2-6: Schematic representation of two hypothetical scenarios depicting inter-relationship between *Kerma* and *Absorbed Dose*.

Figure 2-6(a) shows the *kerma* and the *dose* as a function of depth for a hypothetical case where the photon beam is not attenuated at all. In this case the kinetic energy released to the medium by the photon beam (dotted line) remains constant with the depth in the medium, and the same number of electrons is set in motion in each one of the regions A through H. The absorbed *dose* is zero at the surface, since the photon beam will need to penetrate a certain distance into the material before it first interacts. As a certain number of electrons leaves A, they

deposit a little bit of energy here, so the *dose* increases by a little, but most of the kinetic energy is taken downstream. In A there are no electrons coming from above replacing the ones that take kinetic energy out of this section. In B, there is the same number of secondary electrons being set in motion as in A, and these electrons take most of their energy further downstream, but now there are the electrons from A coming through B and depositing some of their energy here as well. Thus the *dose* deposited in B is going to be higher than in A. In C the *dose* deposited will be even higher, since although the same number of electrons takes the same amount of energy out of C as out of A and B, now there are electrons coming from upstream, from both A and B depositing energy in C. In section D the electrons that started in A come to rest and all of the ways through which electrons deposit their energy are present (i.e. the first section where all of the symbols *, \, /, and | are present). Thus *electronic equilibrium* is first attained in D, since the amount of kinetic energy taken out of this section is perfectly balanced by the amount being deposited from upstream, and the *dose* deposited is equal to the *kerma*. This will be true for all the subsequent sections E to H and beyond [1, 3]. As indicated on Figure 2-6 the region from the surface of an irradiated medium to the depth of *electronic equilibrium* is called the *buildup region*.

Figure 2-6 (c) presents the more realistic case where the photon beam undergoes some attenuation. Now the *kerma* will decrease constantly as there are less and less photons in the beam releasing energy. The *dose* increases in much the same way as for the no attenuation case, but past the *buildup region*, the *dose* is consistently higher than the *kerma* (if radiative losses are not taken into account or are considered negligible), and strict electronic equilibrium is no longer attained. The lack of an electronic equilibrium past the *buildup region* is due to the fact that, as noted in the previous section, the *kerma* and absorbed dose do not take place at the same location. If the photon beam attenuation is taken into account, at any point in a medium, past the buildup region, there will be slightly more electrons coming to rest and depositing their kinetic energy from upstream than electrons leaving and taking kinetic energy away [3, 4].

2.4. Radiation Induced Current (Compton Current)

For the range of energies typically used in radiotherapy (1 to 10 MeV) the Compton interaction dominates, as can be seen from Figure 2-1. The Compton electrons produced as a result, are preferentially forward scattered [5, 6] and can give rise to a directional current in dielectrics irradiated by a high energy photon beam [7]. If the irradiated medium is a conductor with a thickness smaller than the average range of the Compton electrons, the conductor experiences a net electron loss, since most electrons set in motion by the Compton process are ejected from it. As a result a net positive charge is left behind. If the conductor is connected to a circuit electrons flow from the circuit to restore charge balance and the so called *radiation induced current* (RIC) or *Compton current* appears. The RIC has been found to be the main cause of the voltage independent polarity effect in parallel plate ionization chambers, and to be due to a lack of electronic equilibrium [8]. It has also been suggested that the RIC is responsible for the instantaneous current that appears in the irradiated conductors of RF coils [9].

To remove RIC from a thin conductor (such as the conductor of an RF coil) electronic equilibrium has to be established. This can be done by using a suitable material for buildup. If the buildup material is thick enough and has an identical or similar density to the conductor, there will be enough electrons produced in it such that most Compton electrons displaced from the conductor will be replaced by other electrons set in motion upstream and coming to rest in the conductor. Establishing electronic equilibrium, removes the charge imbalance and the need for electrons to flow from the circuit to the thin irradiated conductor, thus effectively removing RIC.

2.5. Electrets

Since Teflon was used for some of the experiments presented in this thesis, and since Teflon is an electret, in this section some properties of this special class of dielectrics will be presented.

2.5.1. Definition and Properties

An electret is usually defined as the electrostatic analogue of a permanent magnet, in that it is a piece of dielectric material that is capable of storing electrostatic fields for long periods of time. The long term storage of electrostatic fields can be caused by surface charge layers, space charges trapped in the material, by a "true" polarization of the dielectric, or by a combination of these. The first materials used to produce electrets were waxes, rosins, and sulphur, and they were usually obtained by cooling the melted substance in the presence of an electrical field. Nowadays, thin films (10 – 50 μm thick) made out of polymers such as Teflon materials or polyvinylidene fluoride, are being used for making electrets. The typical electrets in use today have one or both surfaces of the thin film coated with evaporated metal. For the electrets coated with metal on both sides the electric fields are completely contained within the dielectric, while the ones that are not metalized at all, or have only one side metalized, exhibit both internal and external electric fields. Modern electret charging techniques involve the application of high energy ionizing radiation to the dielectric material. Whether bombarding the dielectric material with an electron beam with a smaller range than the dielectric thickness, or using a gamma or high energy x-ray beam, electrets can be charged even without the presence of an electric field [10].

2.5.2. Photon Irradiated Electrets

Charge storage effects, due to microscopic structural defects, macroscopic heterogeneity, electrode polarization, or dipole formation and orientation, are seen in most dielectrics exposed to ionizing radiation. When a beam of x-ray photons with energies above about 0.3 MeV enters an electret, the photons interact

predominantly by the Compton process, creating a preferentially forward scattered flux of Compton electrons. The radiation beam reaches electronic equilibrium only at a depth equal to the maximum Compton electron range. Thus, at the surface of incidence there will be an electron depletion or formation of a positive charge layer, since in the buildup region there are more electrons scattered forward than coming in from above, as previously explained in Section 2.4. If the electret is placed on top of a material with a higher atomic number while being irradiated, an electron excess layer will form on the side opposite to the surface of incidence, where the radiation goes from the electret to the higher atomic number material. This excess of electrons is due to the fact that in this transition region, there will be more electrons backscattered from the high atomic number material into the electret than forward scattered from it [11].

References:

1. F.H. Attix, *Introduction to Radiological Physics and Radiation Dosimetry*, John Wiley & Sons, 1986.
2. http://www.nist.gov/pml/data/xcom/index.cfm
3. H.E. Johns, J.R. Cunningham, *The Physics of Radiology Fourth Edition*, Charles C Thomas, Springfield, Illinois, 1983.
4. A. Nahum, *Handbook of Radiotherapy Physics Theory and Practice*, Edited by P. Mayles , A. Nahum , and J. C. Rosenwald, Taylor & Francis 2007, pp 89 – 115.
5. H.E. Johns, A. Aspin, and G.G. Baker, *Currents Induced in the Dielectrics of Ionization Chambers through the Action of High-Energy Radiation*, Radiation Research **9**, 573 – 588, 1958.
6. R.A. Meyer, F.L. Bouquet, and R.S. Alger, *Radiation-induced conductivity in polyethylene and Teflon*, J. Appl. Phys. **27**, 1012 – 1018, 1956.
7. B. Gross, *Compton Dosimeter for Measurement of Penetrating X-Rays and Gamma Rays*, Radiation Research, **14**, 117 – 130, 1961.
8. Abdel-Rahman, Seuntjens J.P., Verhaegen F., Podgorsak E.B, *Radiation induced currents in parallel plate ionization chambers: Measurement and Monte Carlo simulation for megavoltage photon and electron beams*, Med. Phys. **33** (9), 3094 – 3104, 2006.
9. B. Burke, B. G. Fallone, and S. Rathee, *Radiation induced currents in MRI RF coils: application to linac/MRI integration*, Phys. Med. Biol., **55**, 735-746, 2010.
10. G.M. Sessler, "Introduction", *Topics in Applied Physics Volume 33: Electrets*, Editor: G.M. Sessler, Springer-Verlag Berlin Heidelberg New York, 1980.
11. B. Gross, "Radiation-Induced Charge Storage and Polarization Effects", *Topics in Applied Physics Volume 33: Electrets*, Editor: G.M. Sessler, Springer-Verlag Berlin Heidelberg New York, 1980.

3. Materials and Methods

This chapter discusses the various experimental setups, equipment and methods used for studying the RIC that appears in RF coils. The first set of experiments is designed to study the method of removing or reducing the RIC. Additionally, the experimental procedure for studying the effect of placing the RF coil in the path of the treatment beam on the patient skin dose is illustrated. A simple experiment designed to highlight the difference in the shape of the time-dependent RIC pulse in the presence of a transverse magnetic field is also discussed.

It was established in [1] that the source of the RIC in MRI RF coils is the thin conductor, and in the previous chapter, the RIC was defined as the current resulting from the charge imbalance in thin conductors caused by preferential forward ejection of Compton electrons. It is suspected that the RIC could be caused by the lack of charged particle equilibrium in the thin conductor of the RF coil. Therefore, it is beneficial to study the RIC in thin, flat conductors as opposed to complicated shapes such as those in solenoid or bird cage type of RF coils. Thus a simplified setup, that would enable measuring the RIC in flat conductors in combination with various buildup materials, was used. This simplified approach will determine the proper combination of conductor and buildup material that would, in turn, enable a RIC free RF coil to subsequently be built.

For measuring the effect of the presence of an RF coil in the treatment beam on the patient skin dose, a set of rectangular coil materials were used in combination with a flat solid water phantom. This technique made use of available materials and avoided the necessity of building a special phantom that could fit inside an existing RF coil. Investigating the effect of the transverse magnetic field on the RIC in an RF coil, some of the measurements done in [1] were repeated and then compared to RIC measurements done using the prototype linac-MR system with a magnetic field present.

3.1. RIC Removal

3.1.1. Experimental Setup

The schematic representation of the experimental setup is shown in Figure 3-1. Thin plates of copper and aluminum were used as potential conductors of an RF coil. The RIC in these plates (henceforth called detectors) was measured and subsequently removed or significantly reduced, using sheets of various materials and thicknesses for buildup. A linear accelerator producing bremsstrahlung photons with peak energy of 6 MeV was used to irradiate the detector and buildup combinations.

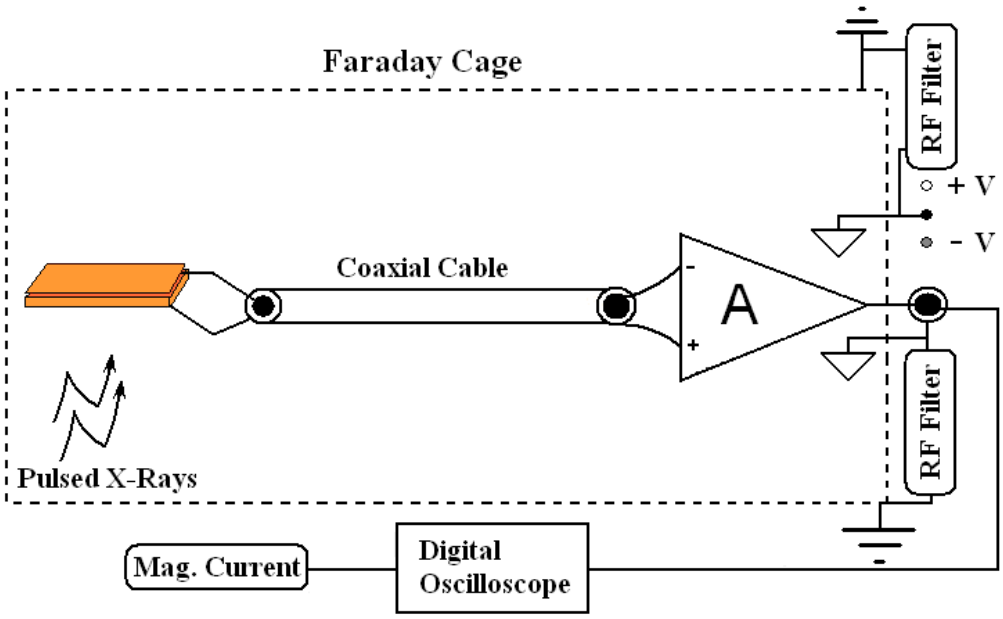

Figure 3-1: Schematic representation of a metal plate inside the Faraday cage (dotted line). The pulsed radiation beam is focused on the plate. The RIC is amplified then detected by a digital oscilloscope, triggered by the linac's magnetron pulses.

The microwave power for this particular linac was supplied to the waveguide by a magnetron. A magnetron is a high power oscillator that uses an intense pulsed DC electric field, applied between the anode and central cathode, in its production of high power microwaves. The pulsed electric field is provided by shaped voltage pulses supplied by the pulsed power modulator to the central

cathode [2]. Both the magnetron and the pulsed power modulator are known to produce significant RF noise in the linac room [3]. Thus, the entire experimental apparatus was placed inside a Faraday RF Cage (Model FC-10, LBA Technologies, Greenville, NC) in order to remove the effect of any RF noise on the measurements of the RIC.

The detector was connected to a high speed low current amplifier (59-179 Edmund Optics), and the radiation beam was focused on the detector through the RF cage, making sure the amplifier was not being irradiated. The RF cage was grounded, and the amplifier was mounted on the inside of the cage with screws, and thus its body was also grounded. The power supply and amplifier output connections were brought outside the RF cage through RF filters. A coaxial cable connected the amplifier output to an Agilent (Agilent Technologies Inc., Santa Clara, USA) DSO6104A digital oscilloscope, which was triggered by the linac's magnetron pulses. The acquired time-dependent signal voltage (i.e. signal trace) was transferred from the oscilloscope to the PC and recorded, using a Keithley KUSB 488 GPIB interface (Keithley Instruments Inc., Cleveland, OH) implemented with the software program DADiSP (DSP Development Corporation, Newton, MA).

For each thickness of buildup material, the mean and standard deviation of the RIC were obtained as follows. A total of 100 time-dependent voltage pulses were acquired in DADiSP. Each pulse contains background signal (no radiation) and voltage pulse during the irradiation. All 100 pulses were then averaged to obtain a single trace. The mean raw RIC and mean background signals were then obtained by time-averaging of the appropriate portions of the trace, i.e. the mean raw RIC was the time-average of uniform portion of radiation induced pulse while the mean background was the time-average of the background trace during the period of no radiation. Finally, the mean RIC was obtained by subtracting the mean background from the mean raw RIC. The standard deviation of RIC was calculated as the standard deviation of the time-averaged, background subtracted RICs obtained from the top, uniform portion of 100 individual traces.

3.1.2. Equipment

In this following section a brief description of the equipment used for this set of measurements is presented.

Faraday RF Cage (Model FC-10, LBA Technologies, Greenville, NC) has a welded aluminum construction, with a high conductivity, bare aluminum interior. The thickness of the aluminum faces is 3.2 mm. It provides up to 70 dB plane wave isolation (typically 50 dB at 1GHz) from 100 kHz to 6 GHz RF range. The easy access door panel is fitted with two handles for portability and handling, and it connects with the RF cage with conductive gasket while closed. The cage size of 61 x 76 x 61 cm^3 is large enough to house the experimental setup and it is light enough (25 Kg) to easily transport between lab and the clinical linac vault [4].

The High Speed Low Current Amplifier (59-179 Edmund Optics) has an input impedance of 50 Ω, variable gain switchable from $1x10^2$ to $1x10^8$ V/A with a maximum bandwidth of 200 MHz (at the lowest gain). Additional filter may be used to limit the upper cut-off frequency to 1MHz, 10 MHz or to the full bandwidth at a given gain setting. It features a switchable AC/DC coupling, and an adjustable bias voltage (±10 V, max. 22 mA) connected to the shield of the BNC input connector, switchable to ground [5]. The amplifier was used with a nominal gain setting of 10^5 V/A (10 MHz bandwidth) in DC coupling mode with the detector bias normally connected to the ground in most experiments.

The Digital Oscilloscope (Agilent Technologies Inc., Santa Clara, USA) is a DSO6104A model. It has 4 analog input channels with the input impedances of either 50 Ω or 1MΩ. To match the output impedance of the amplifier, the 50 Ω input impedance was used for all measurements. With a bandwidth of 1GHz, a sample rate of 4 Giga-samples per second, a memory of 8 Mpts, and an update rate of up to 100,000 deep-memory waveforms per second, this scope allows for very fast acquisitions, detection of infrequent events, and visualization of very

subtle detail, making it ideal for recording the short RIC induced by the pulsed radiation beam of the linac. With all the acquired RIC traces being framed in a 20 μs window, each acquired trace consisted of 80,000 data points. The scope is also capable of performing waveform math like averaging of wave forms. The averaging function was used before most data acquisitions to do a visual check making sure no stray RF was interfering with the desired RIC signal trace.

3.1.3. Detector-Buildup Combinations

All experiments were conducted in the 6 MV photon beam from a 600C (Varian Medical Systems, Palo Alto, CA) linear accelerator. Initially the RIC in copper was evaluated since most RF coils in use today have copper for their conductor. Figure 3-2 shows the actual plate setup for the copper detector, copper buildup measurements.

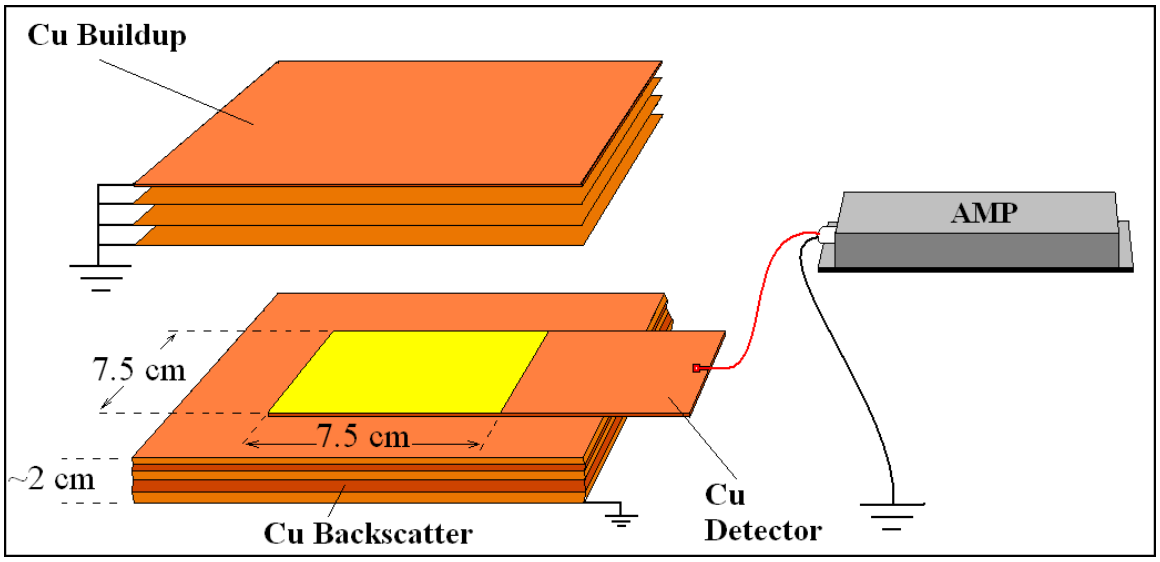

Figure 3-2: A closer look at the copper detector, copper buildup, RIC measurement setup. The backscatter material is ~2 cm of copper, in direct contact with the RF cage, thus grounded. The copper detector is electrically insulated on both sides with electrical tape, and the buildup is grounded as well.

The detector was a 0.12 mm thick copper sheet, wrapped on both sides with 3M Tartan 1710 Vinyl Electrical Tape to electrically insulate it from the rest of the setup. A ~2 cm thick stack of copper plates provided the backscatter. For

this set of measurements, the backscatter copper was in direct contact with the bottom of the RF cage and was thus grounded. The radiation field size was 7.5 cm by 7.5 cm at the surface of the detector, and the distance from the linac's radiation source to the top surface (i.e. SSD) of the backscatter plates was about 123.7 cm. Using the aforementioned setup, the mean amplitude of the RIC was measured as a function of increasing thickness of copper build up plates placed on top of copper detector. The buildup needed to be grounded, since during each radiation pulse, the electrons knocked out from it would leave behind a net positive charge, which in turn would polarize the detector inducing a very short lived electrostatic field. This electrostatic field would prevent the electrons which are barely set in motion within the build up from reaching the detector and the measured RIC (representing a lack of electrons in the detector plate) signal would be higher than expected for a given buildup thickness.

The RIC was also evaluated in aluminum conductor with Teflon buildup. Teflon was used due to its similar density to that of aluminum $\left(\rho_{Al} = 2.7\, g/cm^3, \rho_{Teflon} = 2.2\, g/cm^3\right)$ and due to the fact that it is a non conductive polymer that would not interfere with the function of an RF coil. The detector buildup combination setup for this set of measurements is shown in Figure 3-3. The "detector" was a 0.54 mm aluminum plate, insulated on both sides with the same type of electrical tape used in the copper experiments. The backscatter was provided by a 2 cm thick slab of solid water to somewhat simulate tissue. As before the beam was 7.5 cm by 7.5 cm and the SSD = 123.7 cm. On top of the detector, sheets of various thicknesses of Teflon were placed as buildup. The top and bottom surfaces of the Teflon sheet stack were grounded using a ~ 0.06 mm thick aluminum tape. The mean amplitude of the RIC pulse from about 100 measurements was again recorded for each new thickness of buildup.

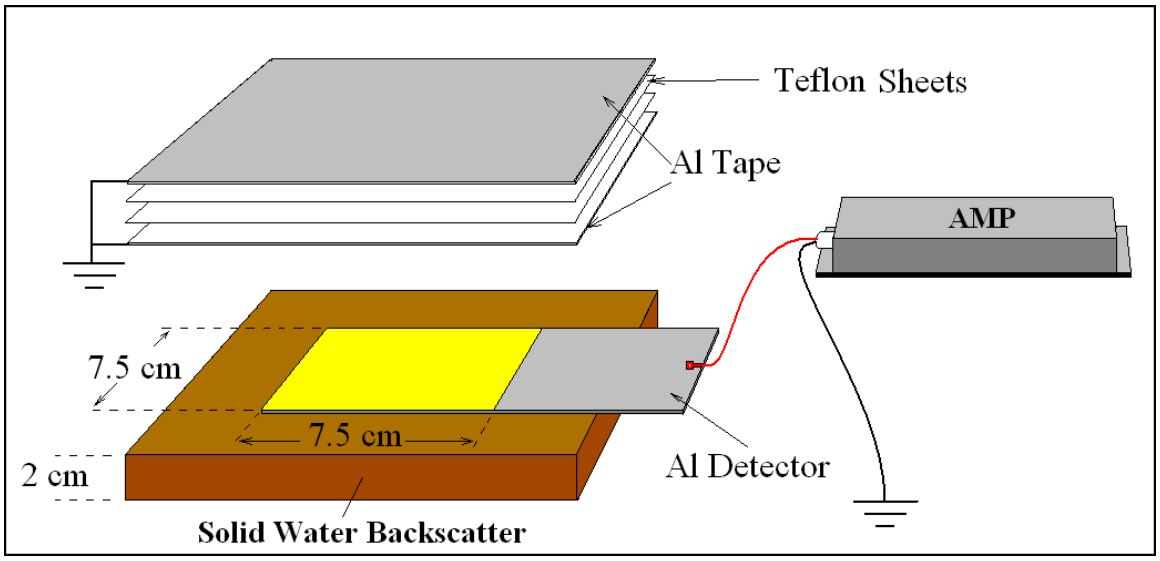

Figure 3-3: A closer look at the aluminum detector, Teflon build up, RIC measurement setup. The backscatter material is 2 cm of solid water. The aluminum detector is again electrically insulated on both sides with electrical tape, and the Teflon build up sheets have grounded aluminum tape on the top and the bottom of the stack.

The grounded aluminum tape on the top and bottom of the buildup material was necessary since Teflon is a very good electret [6], which means that it can store electrostatic fields for long periods of time. An electret can trap some of the Compton electrons and become polarized when under direct irradiation. Thus both an internal and an external electrostatic field appear in Teflon, as was explained in Section 2.5.2. By using grounded conductive electrodes on the top and the bottom of the buildup stack the external electrostatic field is removed [6, 7]. Also, when using single pieces of thicker Teflon for the buildup, although with the grounded aluminum tape in place, the RIC readings would become erratic (i.e. would not follow an expected trend with increasing buildup thickness) after a certain number of monitor units (1 MU = 1cGy delivered to water at a point 100 cm away from the source with a depth of 1.5 cm using a 10 cm x 10 cm field size) was delivered. This variation among multiple readings, depending upon the prior irradiation history of Teflon, for the same buildup thickness was due to the charging of the Teflon buildup. The type of Teflon buildup that yielded consistent results was a stack of about ten, 0.9 mm thick, Teflon sheets, loosely stacked, with grounded aluminum tape on the top and bottom of the whole stack (i.e. the

aluminum tape was on the bottom of the bottom sheet and on the top of the top sheet and all other sheets were slid in between these two as seen in Figure 3-3). Occasionally a thicker piece of Teflon (~5 mm) was added to the stack, in between the 0.9 mm thick sheets (and thus in between the two grounded aluminum tapes), to increase the buildup thickness. For this type of buildup, the same beam that charges the Teflon and induces positive and negative charge layers on the top and bottom side of each one of the 0.9 mm thick sheets will also ionize the air in between the Teflon sheets. Since there is no grounded surface in between the individual sheets of Teflon (just the top and the bottom of the entire stack has the grounded aluminum tape) there will be an electrostatic field in the small air gaps present in between the Teflon sheets. This field will make positive and negative charged ions from the air gaps annihilate some of the negative and positive charge layers, induced on the surfaces of the individual Teflon sheets. So although this type of buildup will get charged as well, the ions produced in the air between the sheets, should deplete at least some of the Teflon's charge layer through annihilation of opposite charge carriers on the surface [8, 9] and thus discharge the buildup at the same time.

Using the detector buildup setup from Figure 3-3, the RIC measurements were subsequently redone using the 0.12 mm thick copper detector and Teflon as the buildup material in order to evaluate the RIC reduction in a case where the density of the build up material is substantially different from that of the detector.

3.1.4. Conductor Thickness

Since the thickness of the copper conductor in RF coils varies between the many types of coils that are in use today, an investigation into how the copper detector plate thickness influences the amplitude of the recorded RIC was also carried out. The setup used for this set of experiments, is shown in Figure 3-4. This setup was similar to the one in Figure 3-2, except there was no buildup used. Instead, on top of a very thin copper detector (about 0.05 mm thick), electrically insulated from the backscatter, plates of various thicknesses of copper were added in direct electrical contact. Direct electrical contact between copper plates

effectively increased the detector thickness. The beam size was kept at 7.5 cm x 7.5 cm and the SSD at 123.7 cm to the surface of the backscatter. The average amplitude of about 100 RIC traces was recorded for each new detector thickness.

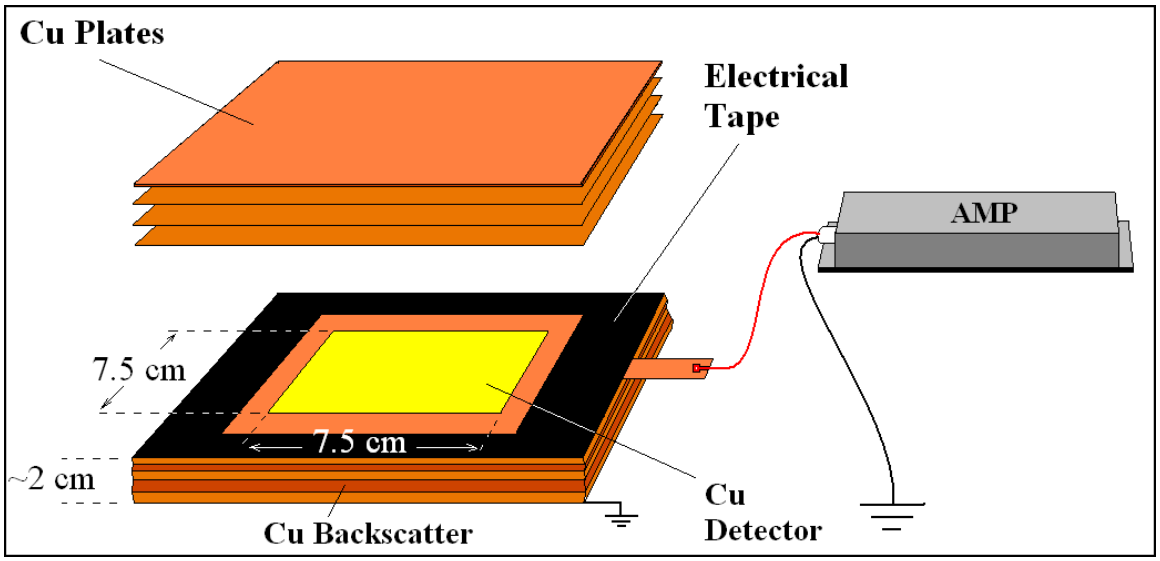

Figure 3-4: A closer look at the influence of conductor thickness on RIC amplitude measurement setup. The backscatter material is ~2 cm of copper, in direct contact with the RF cage, thus grounded. The copper detector is electrically insulated on the bottom side with electrical tape, and copper plates are added on top in direct electrical contact to increase the detector thickness.

3.1.5. Influence of Backscatter

MRI surface coils are placed directly in contact with the patient while there may be an air gap between the coil and the patient surface in other types of coils. Thus the placement of the backscatter material in direct contact with the detector in aforementioned experiments only simulates the scenario of surface coils. This experiment was conducted to compare the surface coil type scenario to the non-surface coil. It was done by changing the type of backscatter material in the RIC experiments.

The influence of the backscatter material on the RIC measurements was first investigated for the copper detector, and copper and Styrofoam backscatter materials were compared. The two backscatter setups are schematically represented in Figure 3-5.

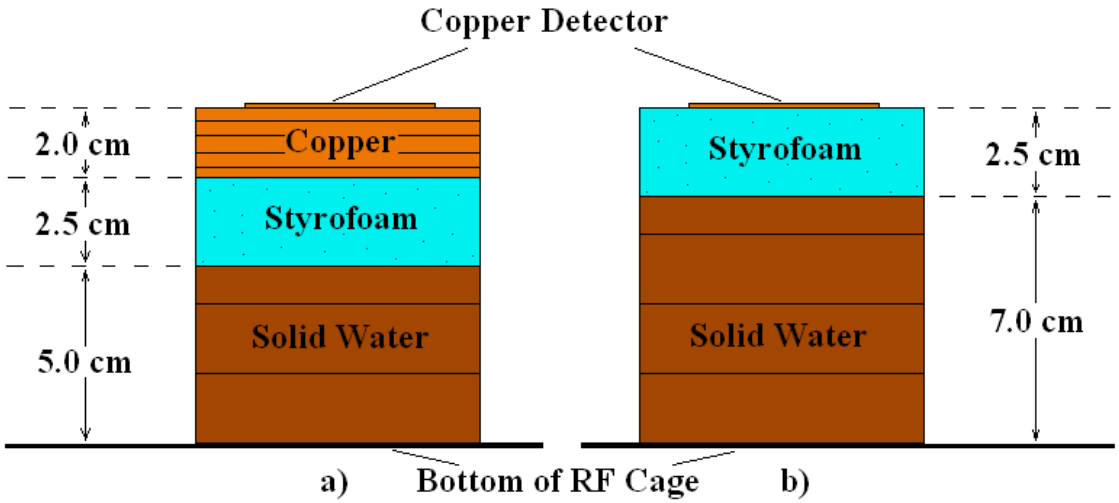

Figure 3-5: Schematic representation of the two types of backscatter used.

First, the RIC was measured with the same setup as in Figure 3-2, only the whole setup was placed on top of a 2.5 cm thick block of Styrofoam that was sitting on top of 5 cm of solid water (Figure 3-5.a). This first combination of backscatter materials was used to simulate the patient, and the distance between the patient and a coil built with copper for the conductor backscatter. Since the SSD to the bottom of the RF cage was 125.7 cm the new SSD to the surface of the backscatter material was about 116.2 cm. Then the 2 cm of copper back scatter were replaced with the 2.5 cm of Styrofoam sitting on top of 7 cm of solid water this time, thus preserving the same SSD (Figure 3-5.b), and the RIC measurements were retaken.This second combination of backscatter materials was used to somewhat simulate the patient as well as the distance between the patient's body and the RF coil conductor, this time built with virtually no backscatter. Grounded copper plates were again used as buildup material and the RIC was measured as a function of thickness of copper buildup plates.

The influence of the backscatter material on the aluminum detector RIC measurements was investigated next. A very similar set of setups to the ones used for the copper detector and schematically represented in Figure 3-5 was used. First the setup of Figure 3-3 was placed on top of 2.5 cm of Styrofoam sitting on 5

cm of solid water, similar to Figure 3-5.a. In this case, the 2 cm of copper backscatter seen in Figure 3-5a was replaced by 2 cm of solid water and the 0.54 mm thick aluminum detector replaced the copper detector. This particular backscatter setup simulates an aluminum coil placed directly on top of a patient. The next setup was identical to Figure 3-5.b with 2.5 cm of Styrofoam sitting on top of 7 cm of solid water making up the backscatter, and the aluminum detector in place of the copper one. This backscatter setup was used to simulate, as before, an aluminum coil, built with basically no backscatter, placed a distance away from the patient. A third type of backscatter was investigated, for the aluminum detector. This case was similar to the one depicted in Figure 3-5.a with about 2 cm of Teflon, with grounded aluminum tape on the top and bottom, replacing the 2 cm of copper in the backscatter materials. Thus, from top to bottom, the backscatter was 2 cm of Teflon, on top of 2.5 cm of Styrofoam, on top of 5 cm of solid water. This third backscatter setup was meant to simulate an aluminum RF coil, built with the conductor practically embedded in Teflon, and placed a distance away from the patient. The same SSD of 116.2 cm, as for the copper detector measurements, was maintained, and the same Teflon from the previous set of measurements, with grounded aluminum tape on the top and on the bottom of the sheet stack, was used. For all the measurements in this section, the field size was readjusted to the new SSD such that it was still 7.5 cm by 7.5 cm at the detector surface.

3.1.6. Aluminum Surface Coil

Figure 3-6 shows the measurement setup used for investigating the RIC reduction in an aluminum surface coil using grounded Teflon as buildup material. The aluminum surface coil was cut from a 1.6 mm thick aluminum plate, tuned to about 8.85 MHz, and provided approximately 43 Ω unloaded impedance at the tuning frequency. The shape and size of the RF coil is shown in Figure 3-7.a and a schematic of the tuning and matching circuit is shown in Figure 3-7.b. Again, for backscatter, about 2.5 cm of Styrofoam on top of 7 cm of solid water was used to simulate the patient as well as the air gap between the coil and the patient.

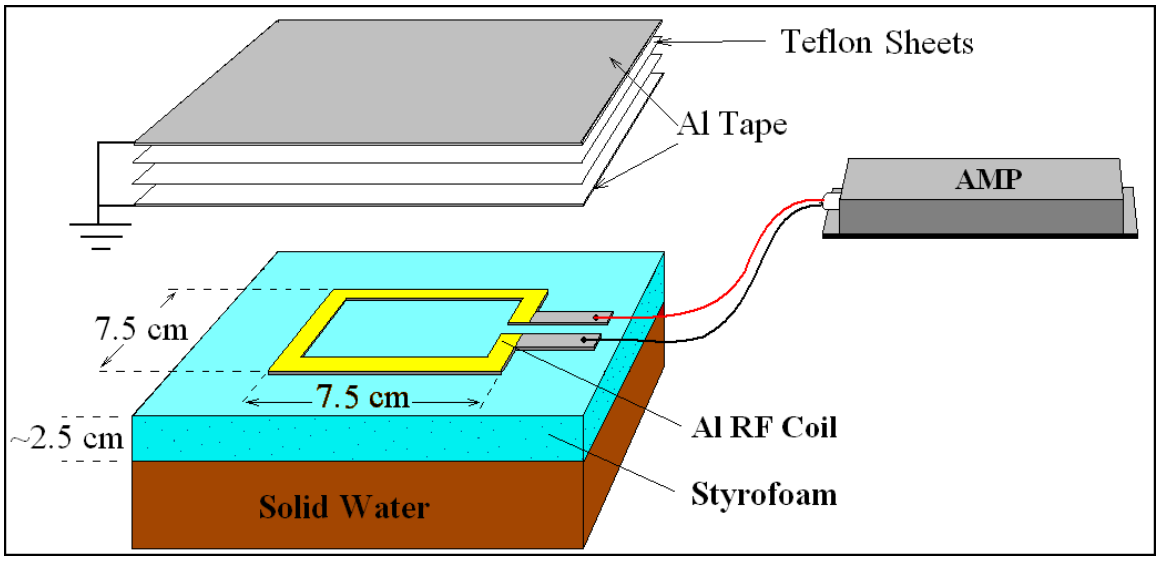

Figure 3-6: Aluminum surface RF coil, with Teflon build up, RIC measurement setup.

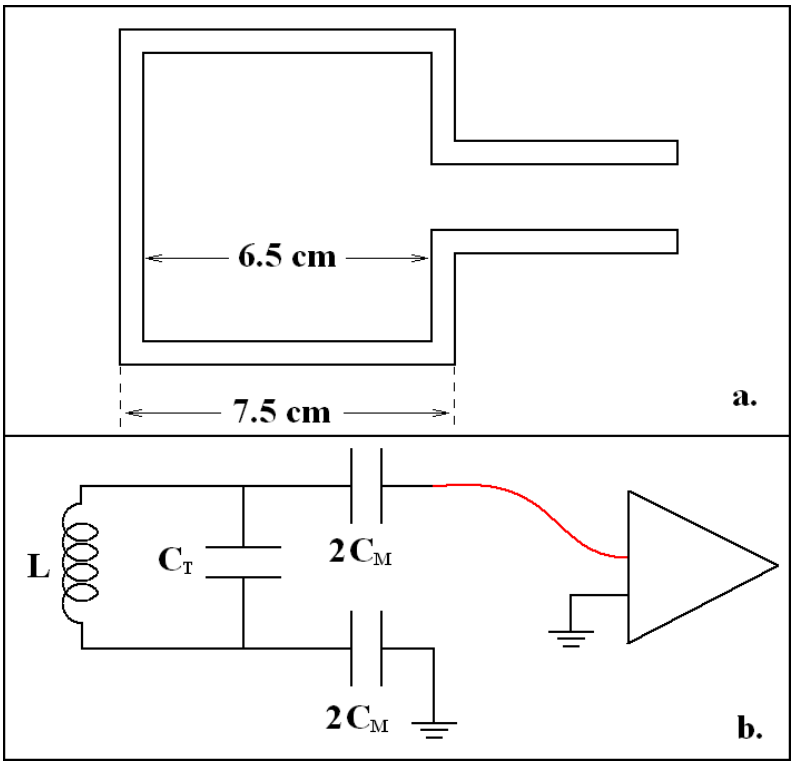

Figure 3-7: Schematic representation of the aluminum surface RF coil built for the measurements. a) shape and dimensions of the coil; b) schematic diagram of the tuning and matching circuit.

For buildup the same sheets of Teflon, with grounded aluminum tape covering the top and the bottom of the stack, from the previous measurements, were used. As before, the beam size was 7.5 cm by 7.5 cm at the surface of the backscatter, with an SSD of 116.2 cm to the top of the backscatter material. The average amplitude of about 100 RIC traces was recorded for each new build up thickness.

3.2. Skin Dose Measurements

The bremsstrahlung beams of medical linacs produce poly-energetic photons with peak energy in the MeV range. As discussed in Chapter 2, these photons eject electrons that can travel further down from the points of interaction within the patient. By this virtue the therapeutic photon beams are characterized by a buildup region as the beam enters and travels through the patient. The dose deposited to the skin is thus considerably smaller than the therapeutic doses delivered to the tumor. Since the skin is an early reacting and highly radiation sensitive tissue, adverse skin reactions largely limited the therapeutic doses to deep seated tumors when using kilo voltage beams. Thus, MeV range photons not only provide useful beam intensity to the deep seated tumors but also the extremely useful skin sparing in radiation therapy. However, the placement of an RF coil either in direct contact or with a small gap between the coil and the patient can potentially lose the skin sparing provided by the megavoltage beams. The following experiments were carried out to study the influence on the skin dose of placing the RF coil, alone or in combination with the build up materials, in the treatment beam. Again the coil and build up materials were emulated by flat sheets for materials to keep a simple experimental set up.

Figure 3-8 shows the measurement setup used to determine the skin dose effects that a coil, whether with or without buildup, would have if present in the radiation beam.

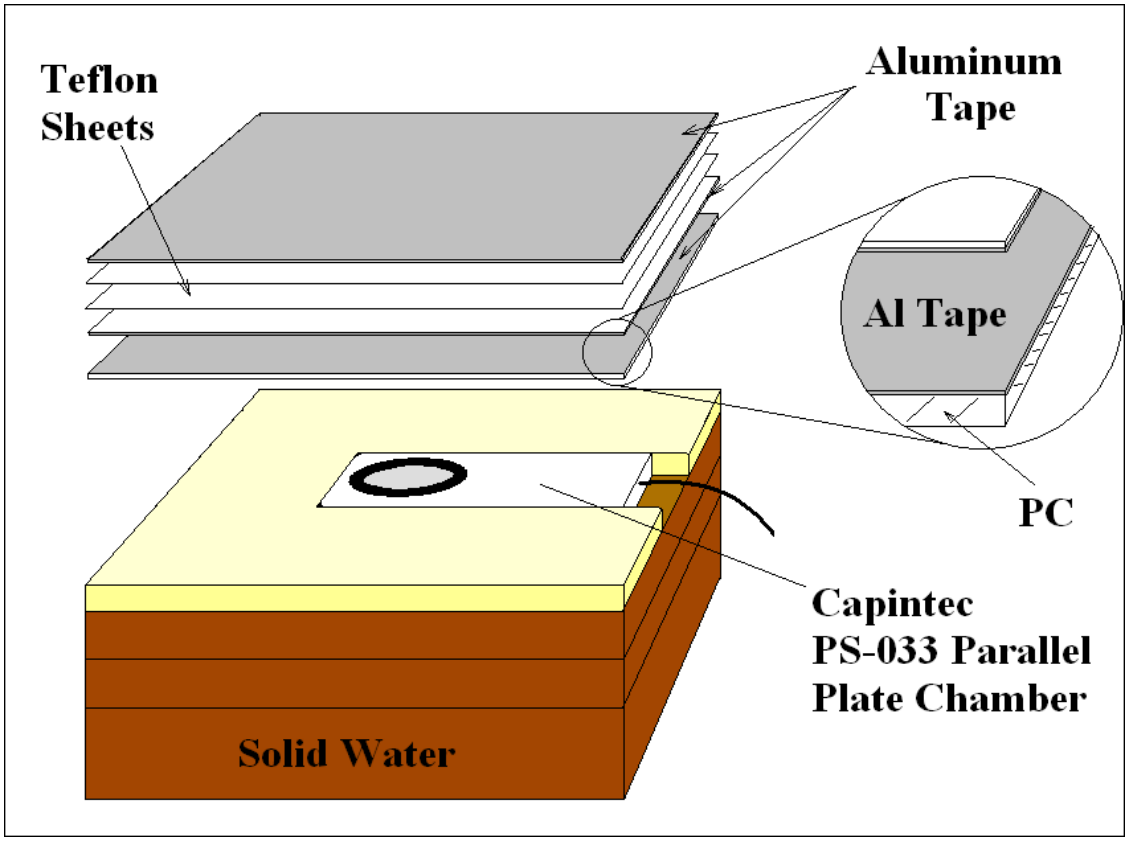

Figure 3-8: Influence of RF coil materials on patient skin dose measurement setup.

A Capintec PS-033 parallel plate ion chamber, embedded in a block of solid water was first used to measure the percent depth dose (PDD) with a Varian 600C linac, using 100 cm SSD to the surface of the solid water phantom, and a 10 x 10 cm^2 field. Sheets of various thicknesses of solid water were added on top to increase the depth of measurement point while the couch that supported the apparatus was moved down such that the SSD was kept at 100 cm. Two readings were taken using a Capintec 192A Digital Dosimeter for each depth of the chamber in the solid water phantom and averaged. Each reading collected the ionization charge in the chamber for 20 MU's where 1 MU represents a dose of 1 cGy at 1.5 cm depth in this experimental set up. This data is denoted as the open beam PDD and represents the dose as a function of depth in a simplified, uniform surface patient of rectangular shape. These measurements were subsequently retaken with various, so called, *coil materials* in the path of the treatment beam,

placed at various distances from the phantom. Three types of coils were simulated with the materials used. First, a sheet of Poly Carbonate (PC), about 1.5 mm thick, with a 0.08 mm thick copper tape on top and a 0.9 mm thick sheet of Teflon on top of the copper (Figure 3-9, a), was used to simulate the backing, conductor and cover, respectively, of a regular copper conductor RF coil.

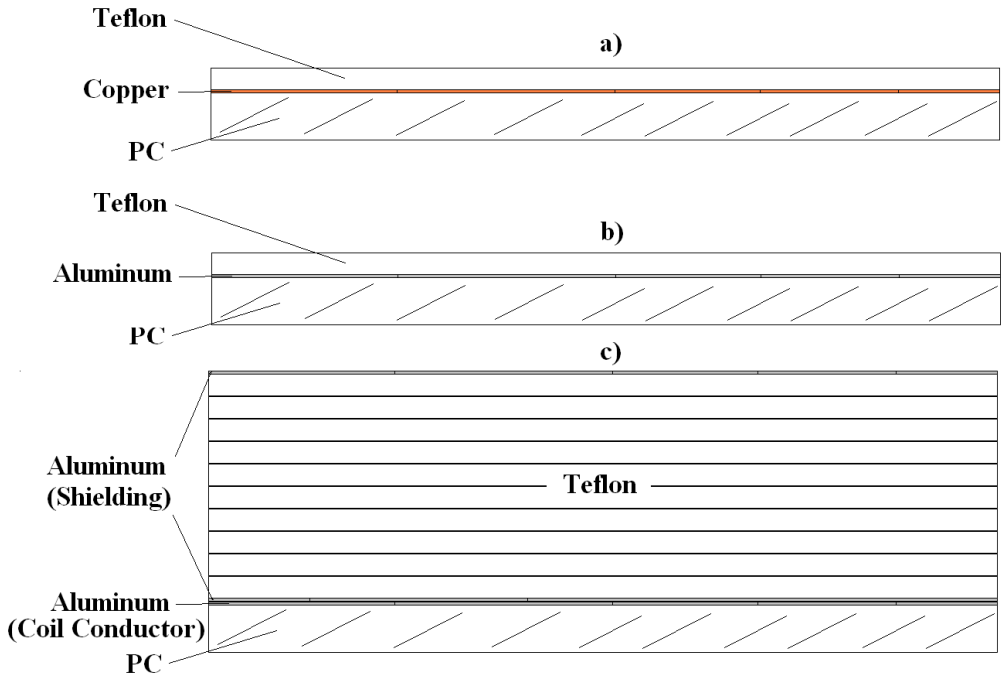

Figure 3-9: Schematic representation of the three types of *coil materials* used to investigate the skin dose effects: a) regular copper conductor RF coil; b) regular aluminum conductor RF coil; c) reduced RIC aluminum conductor RF coil.

Second, another sheet of Poly Carbonate of exactly the same thickness as before, with a 0.06 mm thick aluminum tape on top and the same 0.9 mm thick sheet of Teflon on top of the aluminum was used to simulate the backing, conductor and cover, respectively, of a regular RF coil built with an aluminum conductor (Figure 3-9, b). For the third type of coil simulated, on top of the Poly Carbonate sheet with aluminum tape, a stack of 9 mm of Teflon, with aluminum tape on the top and the bottom of the stack was placed (Figure 3-9, c). This was the same Teflon used previously to reduce the RIC in the aluminum detector plate

measurements, and was used to simulate an RF coil built with an aluminum conductor and Teflon buildup.

PDDs were measured with all these coil materials in direct contact with the surface of the solid water phantom, simulating the effect of a surface coil on the skin dose. In all the PDD measurements, the depth of measurement refers to the depth of the chamber in the solid water phantom excluding the coil material, where the solid water emulates the patient. Thereafter the PDD measurements were repeated with the coil materials at distances of 1 cm, 2 cm, 3 cm, 5 cm, and 10 cm away from the surface of the solid water phantom, to study the effect of an air gap between the coil and the patient on the skin dose (i.e. surface dose in the solid water phantom).

Parallel plate ion chambers exhibit a polarity effect in the buildup region when exposed to a beam of high energy photons. Fundamentally, the Compton electrons leaving the collector electrode of the ion chamber are not replaced by those generated in the buildup material. Thus the electrode not only measures the ions created in the air but also the lack of electrons in the conductor itself. This polarity effect causes the absolute magnitude of the measured ionization current to be higher if the electrode is biased to collect positive ions than the opposite case, thus, causing the change in charge collected when the polarity of the chamber's biasing voltage is reversed [10]. To eliminate the polarity effect and be able to calculate the true ionization current (I) the following formula is used:

$$I = \frac{I_+ - I_-}{2} \tag{3-1}$$

Where I_+ and I_- are the ionization currents measured with a positive and a negative biasing voltage respectively. This process cancels the effect of lack of electrons in collector electrode caused by the Compton current. The measurements taken with the Capintec 192A Digital Dosimeter, which could only provide a +300V bias voltage, did not take into account the polarity effect. Thus, a few of the reduced RIC aluminum conductor RF coil measurements were retaken

with a PTW Unidos E electrometer/dosmeter (PTW Freiburg, Germany) capable of switching the bias voltage between +300 V and -300 V. The purpose of this experiment was to assess the magnitude of the polarity effect on measured PDDs.

3.3. Linac vs. Linac-MR RF Coil Measurements

In order to determine the influence of the transverse magnetic field on the shape of the RIC pulse, the RIC measurements done in [1] were retaken on a Varian 600C clinical linac using the black solenoid RF coil shown in Figure 3-10, and compared to measurements taken using the linac-MR prototype.

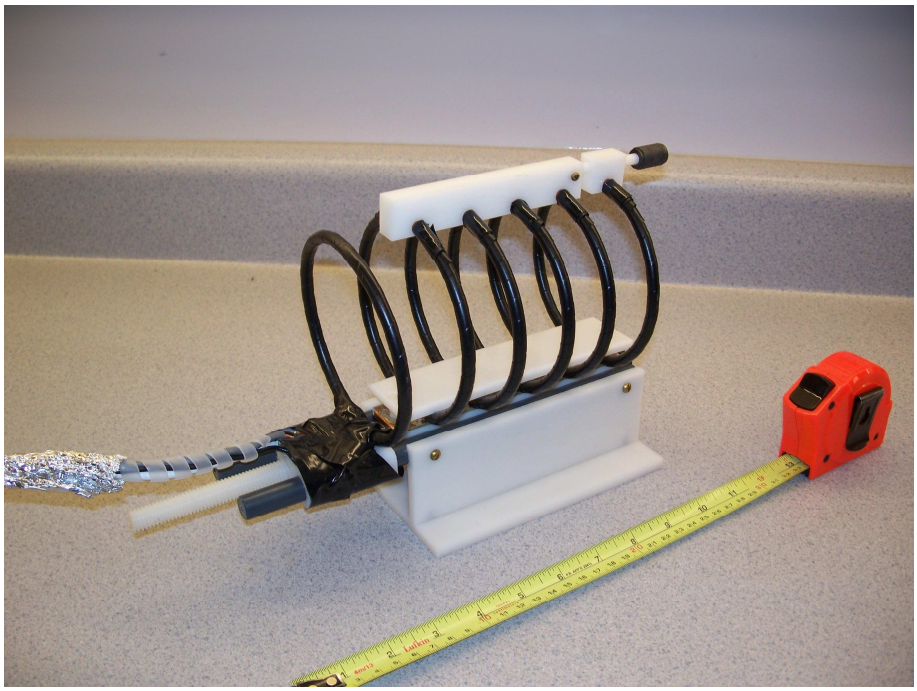

Figure 3-10: The black transmit and receive RF coil used for the linac and linac-MR RIC measurements. The coil is tuned for imaging at 0.22T, and matched at 50 Ω.

The black coil (National Research Council Canada) used for this set of measurements is 12.0 cm long, and has a 10 cm inner diameter. The coil's rings are made of hollow copper pipe, about 0.64 cm in diameter. Five of the rings are connected in series with a capacitor between one ring and the next, thus providing

a solenoid structure. The sixth copper ring has an 820 pF capacitor and is used to inductively match the coil. The black coil is a transmit/receive coil with a tuning range between 9.2 MHz and 9.4 MHz, and was designed specifically for a 0.22 T MRI.

For the clinical linac measurements the same setup as in [1] was used, and apart for the fact that the black coil was placed on a wooden stand inside the Faraday RF cage (Model FC-10, LBA Technologies, Greenville, NC), the setup is identical to the one described for the RIC removal experiments. The distance from the source of radiation to the centre of the black coil was about 115 cm, and the field size was 40 cm by 40 cm at the isocentre.

The setup used for the linac-MR measurements is schematically represented in Figure 3-11.

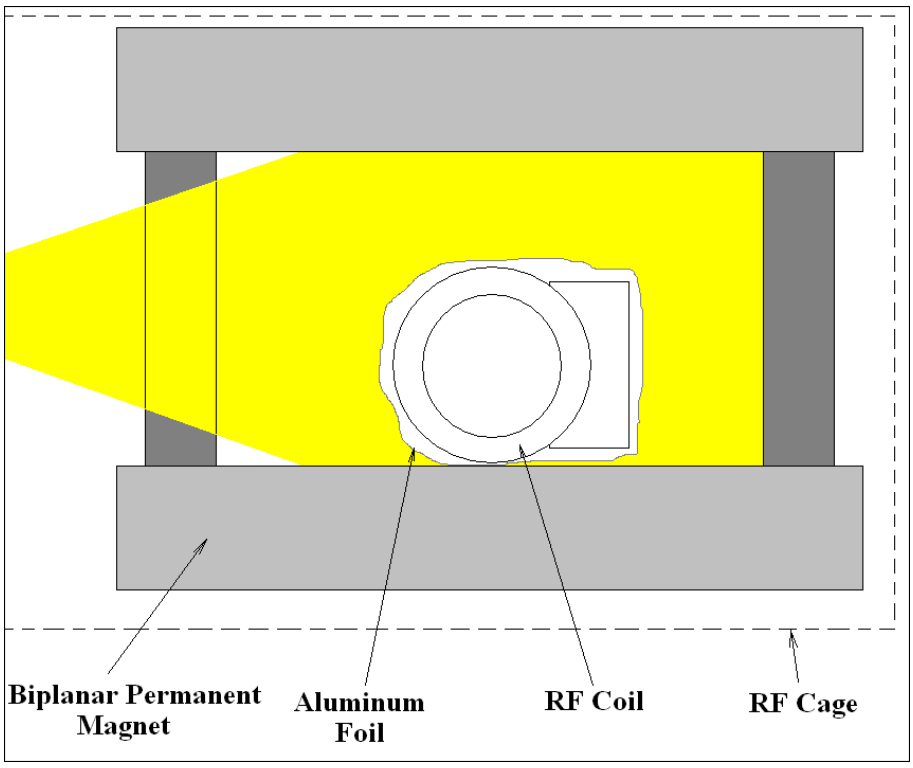

Figure 3-11: Schematic representation of the setup used for the linac-MR RIC measurements using the black coil.

The RF coil was placed inside the biplanar permanent magnet on its side so that the radiation beam would hit it at the same angle as for the clinical linac

measurements. The coil was connected to the same high speed low current amplifier (59-179 Edmund Optics) that was used for the previous set of experiments, and both were inside the linac-MR's RF cage. The amplifier was connected to the digital oscilloscope (Agilent Technologies Inc., Santa Clara, USA) triggered to the linac's magnetron pulses, and the RIC traces recorded on the PC using DADiSP (DSP Development Corporation, Newton, MA). To obtain cleaner measurements the whole coil was wrapped in thin, grounded, aluminum foil, which removed some stray RF that was still present. The distance from the source to the centre of the black coil was about 80 cm, and the field size was large enough to encompass the whole coil for this set of measurements.

For both the linac and the linac-MR measurements the amplifier was placed outside the radiation beam, thus not irradiated, and about one thousand individual RIC traces were recorded and averaged.

It should be noted that the linac used in the linac-MR set up is the same as used in Varian 600C clinical linac. All the ancillary hardware and software is also identical in the two systems. However, the geometric distance from the source to the coil can not be the same in the two experiments due to the placement of the permanent magnet. Also, the dose per pulse in the linac-MR may not be the same as in the clinical linac since no formal attempt has been made to calibrate the doses from the re-furbished linac in the linac-MR system. Although both linacs use the same waveguide, the dose per pulse is a strong function of electron gun current and of the microwave power maintained in the waveguide. These two parameters are different in the two systems for various reasons making the dose per pulse different. These measurements were performed to investigate the influence of the magnetic field on the shape of the RIC pulse rather than to quantitatively evaluate the difference in the amplitude of the RIC pulses in two systems.

References:

1. B. Burke, B. G. Fallone, and S. Rathee, *Radiation induced currents in MRI RF coils: application to linac/MRI integration*, Phys. Med. Biol., **55**, 735-746, 2010.
2. C.J. Karzmark, and N.C. Pering, *Electron Linear Accelerators for Radiation Therapy: History, Principles and Contemporary Developments*, Phys. Med. Biol., **18**, 321-354, 1973.
3. B. Burke, M. Lamey, S. Rathee, B. Murray and B.G. Fallone, *Radio frequency noise from clinical linear accelerators* Phys. Med. Biol., **54**, 2483–92, 2009.
4. http://www.lbagroup.com/technology/faraday-cages.php, Copyright 2009. LBA Group, Inc.
5. http://www.edmundoptics.com/images/imagelib/ds59179.pdf, EO-59-179_2/R 2/SP/11Oct06.
6. G.M. Sessler Introduction, *Topics in Applied Physics Volume 33: Electrets*, Editor: G.M. Sessler, Springer-Verlag Berlin Heidelberg New York, pp 1-10, 1980.
7. B. Gross Radiation-Induced Charge Storage and Polarization Effects, *Topics in Applied Physics Volume 33: Electrets*, Editor: G.M. Sessler, Springer-Verlag Berlin Heidelberg New York, pp 217-278, 1980.
8. B.G Fallone. and E.B Podgorsak, *Production of foil electrets by ionizing radiation in air*, Physical Review B **27** (4), 2615 – 2618, 1983.
9. B.G Fallone. and E.B Podgorsak, *Dynamics of radiation-induced charging and discharging of foilelectrets*, Physical Review B **27** (8), 5062 – 5065, 1983.
10. Abdel-Rahman, J.P Seuntjens, F Verhaegen., E.B. Podgorsak, *Radiation induced currents in parallel plate ionization chambers: Measurement and Monte Carlo simulation for megavoltage photon and electron beams*, Med. Phys. **33** (9), 3094 – 3104, 2006.

4. Results

4.1. Detector-Buildup Combinations

Some preliminary results, illustrating the influence of grounding the buildup in the copper detector copper buildup experiments, are presented in Figure 4-1. The setup for this set of measurements was identical to the one described in Figure 3-2, however a 1.1 mm thick copper detector was used. Three typical RIC traces are presented, and for two of them some RF noise interference can be observed right before and right after the RIC pulse. The only difference between the red trace and the green trace is the grounding of the buildup when the green trace was acquired. It can be seen that the same amount of buildup which, when grounded, reduces the RIC to below zero amplitude, barely manages to reduce the RIC by about 30% when not grounded.

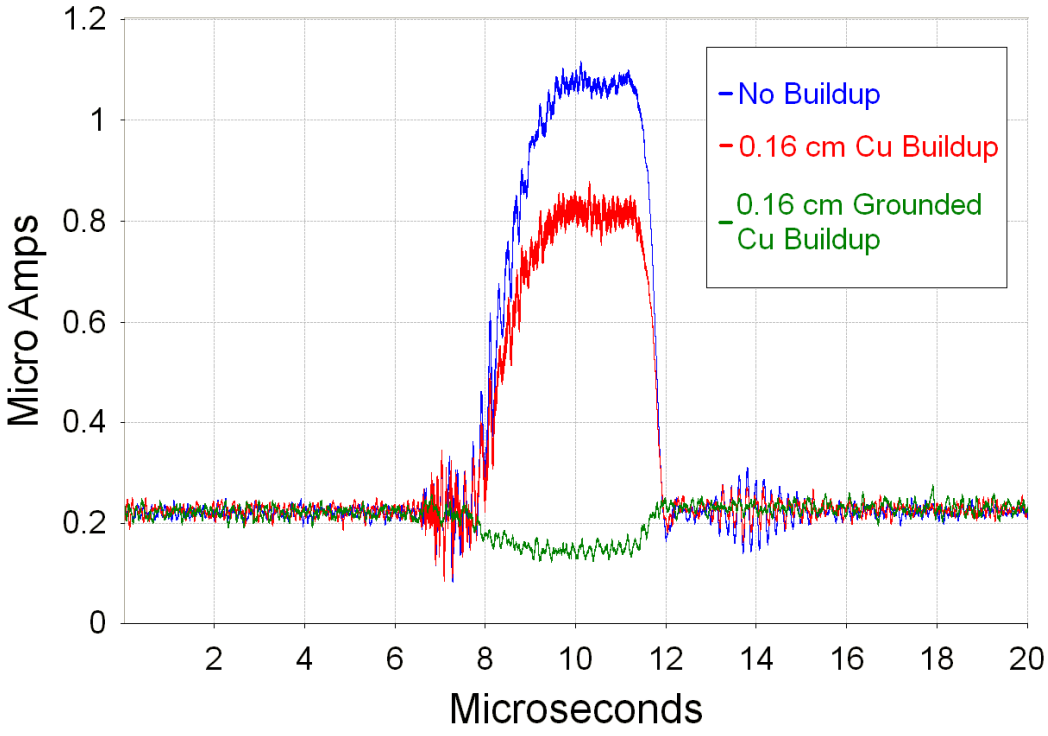

Figure 4-1: Preliminary measurements of RIC in copper, illustrating the influence of grounding the buildup on the RIC reduction.

A very similar set of traces was obtained for the aluminum detector when the Teflon buildup was not placed in between two grounded electrodes. For the case where the Teflon did not have the grounded aluminum tape on the top and on the bottom the original RIC amplitude would be reduced by less than about 40%, while with the grounded electrodes in place the reduction was approximately 90% for the same thickness of Teflon buildup.

Another set of preliminary results showing the difference between using single pieces of incrementally thicker Teflon and using the stack of 0.9 mm thick Teflon sheets for buildup in the aluminum detector measurements is presented in Figure 4-2. These experiments were performed using the same setup described in Figure 3-3, with a 1.3 mm thick aluminum detector and a field size of 7.2 cm by 7.2 cm. The single pieces of Teflon buildup were wrapped in grounded aluminum tape, while the 0.9 mm thick sheets had grounded aluminum tape on the top and on the bottom of the whole stack.

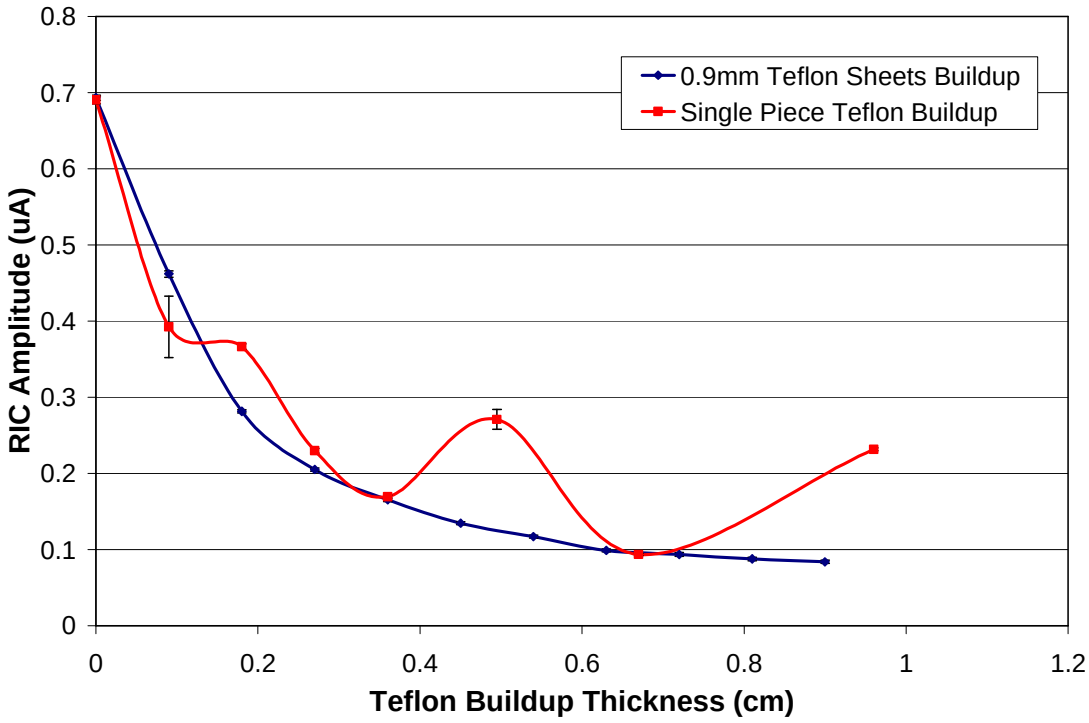

Figure 4-2: Preliminary measurements of RIC in aluminum, comparing the use of thin sheets of Teflon as opposed to single pieces of increasing thickness.

The measured RIC amplitudes using the single, thick Teflon pieces for buildup would fluctuate, and after a few hundred monitor units had been delivered, the RIC reduction curve would look like the red curve in Figure 4-2. This effect persisted even after weeks of not irradiating the single pieces of Teflon used for buildup.

The stack consisting of ten 0.9 mm thick Teflon sheets (with grounded aluminum tape on the top of the top sheet and on the bottom of the bottom sheet) yielded consistent results over and over, and all of the measurement results presented henceforth with Teflon for buildup, were measured using these sheets.

The RIC was measured in a simplified setup in order to better understand its origin. Figure 4-3 shows the mean (see §3.1.1) measured RIC amplitude (μA) as a function of buildup thickness for the various combinations of detector and buildup materials used. The standard deviation (see §3.1.1) of measured data points was, in most cases, smaller than the data markers, for the scale used.

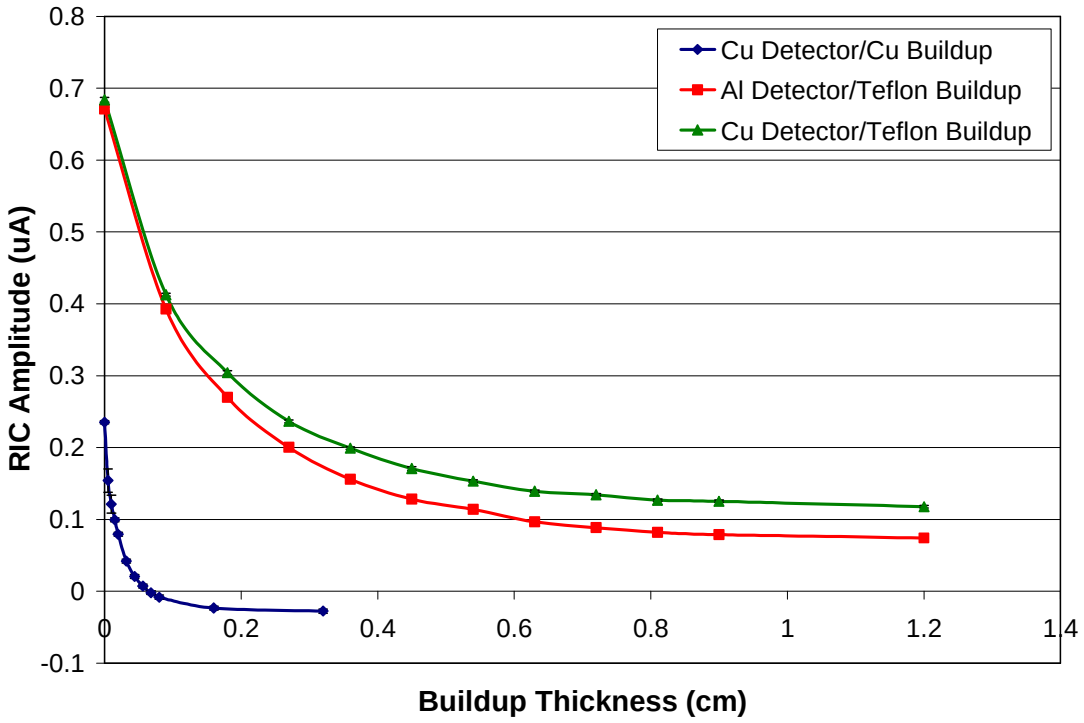

Figure 4-3: Measurement results for the reduction of RIC by buildup for the various detector/buildup combinations used. The error bars in the data points are in most cases smaller than the data markers.

It appears that as the buildup thickness is increased the RIC amplitude decreases indicating electronic dis-equilibrium in the detector as the cause of this observed current. Figure 4-3 clearly shows that by using buildup, and re-establishing electronic equilibrium in the detector plates, the RIC can be removed completely, if the buildup and detector materials are identical. This is precisely the situation for the copper detector/copper buildup combination, and Figure 4-3 shows this to be the only case when the RIC reaches zero amplitude. In the aluminum detector, the RIC is reduced significantly by about 1.2 cm of Teflon buildup, while in the copper detector the RIC can only be partially reduced by the same amount of Teflon.

Electronic equilibrium was only truly obtained in the copper detector with copper buildup, thus, the RIC value only reached zero amplitude for this combination. To establish electronic equilibrium enough interactions must occur in the buildup to produce a sufficient number of low energy electrons that stop in the detector and balance the electrons leaving it. If the density of the buildup is much lower than that of the detector, electronic equilibrium will never be truly reached at any buildup thickness. This is the case for the copper detector and Teflon buildup, since the measured RIC values do not reach zero amplitude. When the density difference between the detector and buildup is smaller, a significant reduction in the RIC can be obtained as is the case of the aluminum detector and Teflon buildup.

For the measurements performed using Teflon for buildup it is expected that some of the charge storage effects described in §2.5.2 are affecting the recorded RIC amplitude. Although sandwiching the Teflon in between two grounded conductive surfaces eliminates most, if not all, of the external electrostatic field, the Teflon itself is still polarized and will have an internal electrostatic field [1]. Up to a depth equal to the maximum range of electrons in Teflon, the Teflon buildup itself is in the electronic dis-equilibrium region. In a thin layer on the top side, where the photon beam is incident, there will be more electrons leaving the layer than coming into it, thus a net positive charge buildup will appear. In another thin layer, on the opposite side of the Teflon buildup, since

the radiation is passing from Teflon to either aluminum or copper, which have higher densities, slightly more electrons are getting backscattered into the layer than forward scattered from it. This leads to the formation of an electron excess layer on the bottom side of the Teflon buildup. Between these two layers there is an electrostatic field that opposes the forward movement of electrons [2]. This field has the potential to prevent some of the very low energy Compton electrons from leaving the buildup and reaching the detector. Since the positive value of RIC in the detector indicates loss of electrons in the detector, the measured RIC amplitude for any given buildup thickness irrespective of the detector material is higher than expected (i.e. if just electron transport without any electrostatic field is taken into account) because of the inability of very low energy electrons to reach the detector.

For the copper detector/copper buildup case, the RIC amplitude actually goes negative after it has reached zero, suggesting that somehow there are more electrons coming into the detector than are leaving it due to Compton interactions. To further investigate this, these measurements were repeated, this time with more copper plates available to provide a thicker (up to 2.7 cm) grounded buildup. The results of this set of measurements are presented in Figure 4-4. Once the RIC reduction curve reaches zero it is seen to quickly go down to a minimum at about 0.8 cm of copper buildup. The measured RIC slowly rises back towards zero if the copper buildup thickness is increased further. This indicates that the measurement setup has a contribution from another current with an opposite polarity to RIC with a magnitude that decreases with increasing depth of the detector within the copper stack.

Suspecting a contribution from the ions created by the radiation beam in the air or electrical tape present between the detector and the backscatter or the detector and the buildup, the copper detector with copper buildup measurements were performed again with both the buildup and the backscatter plates biased at 10V using the high speed low current amplifier on the bias setting instead of ground. Although 10 V is unlikely to attract all the free electrons (created in aforementioned suspected ionizations) away from the detector, it was impractical

to house a higher voltage source in the RF cage. It was assumed that even a 10 V bias, when reversed in polarity, would *detect* the presence of free charges resulting from direct ionizations. The experiment was then repeated with the bias voltage changed to -10 V.

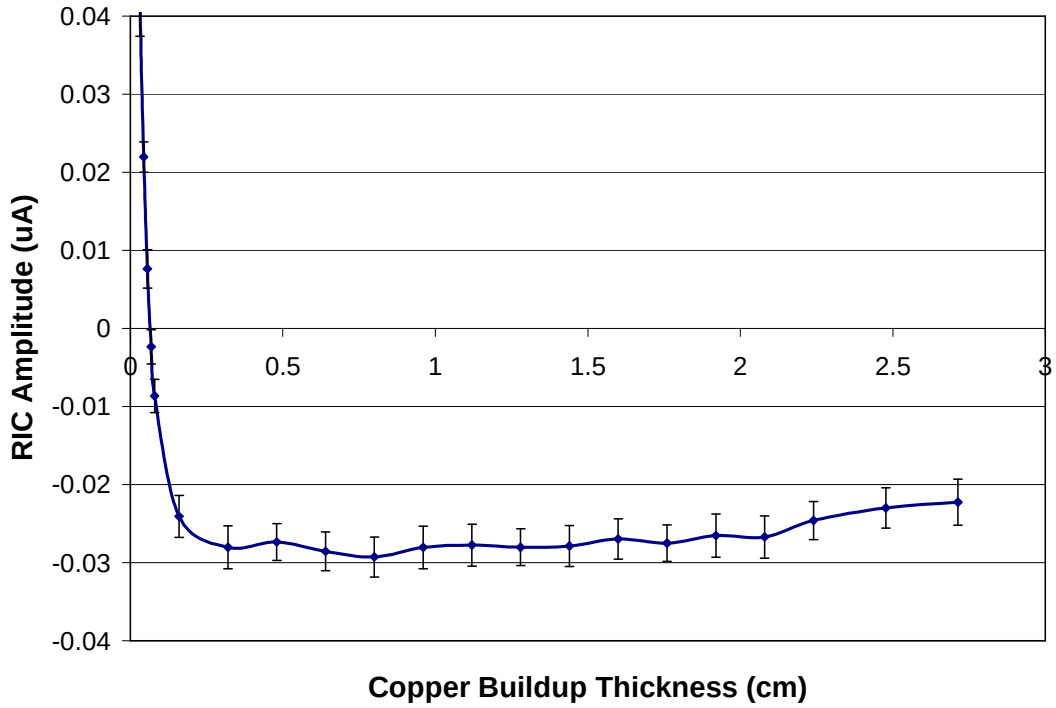

Figure 4-4: Measurement results for the copper detector copper buildup with up to 2.7 cm of copper buildup.

The field size and SSD were kept the same, and for each one of the two polarities about 100 traces were averaged for every buildup thickness. Ionizations would either add or subtract from the measured RIC depending on the detector collecting either positive free charge (buildup and backscatter at +10V) or negative free charge (buildup and backscatter at -10 V) respectively. It was also assumed that a 10 V bias is unlikely to affect the trajectories of Compton electrons in copper stack. Thus, for each thickness of buildup the RIC amplitude was calculated using:

$$RIC = \frac{M_+ + M_-}{2} \tag{4-1}$$

Where M_+ and M_- were the average RIC signal amplitudes measured for the positive and negative polarities, respectively. The average RIC amplitude was calculated and background subtracted as before (see §3.1.1), then compared to the data obtained without the bias voltage present for the copper detector/copper backscatter case. The comparison is presented in Figure 4-5.

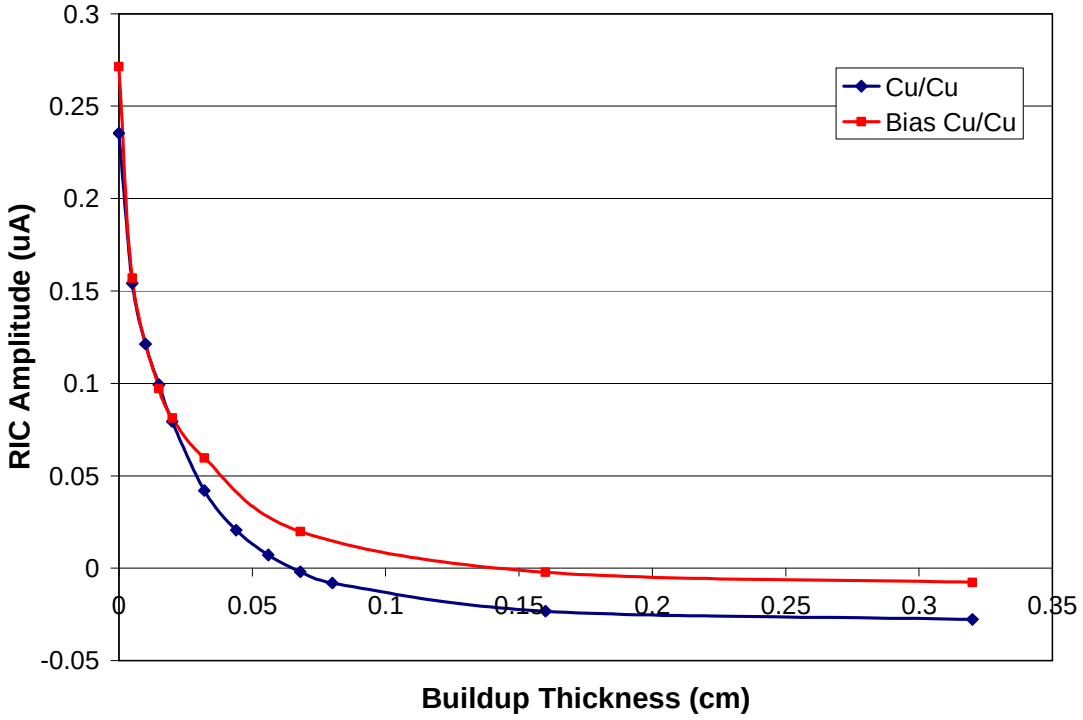

Figure 4-5: Comparison of the copper detector/copper buildup measurements taken with and without the buildup and backscatter biased at ±10 V.

It can be seen from Figure 4-5 that the RIC reduction curve obtained with the reversed bias voltage and using the method described above, has a higher zero buildup amplitude than the curve obtained with no bias voltage. Also the curve measured with the bias reaches zero amplitude slightly below 0.15 cm buildup thickness (closer to the rule of thumb of ~0.16 cm, i.e. depth of maximum dose in water divided by density of copper). One can readily see that the curve obtained with no bias voltage reaches zero amplitude at about 0.07 cm which is significantly smaller than the rule of thumb. For a buildup thickness of 0.32 cm the curve obtained with the reversed bias voltage method barely drops by about

3% of its zero buildup amplitude below zero, compared to a drop of almost 12%, of zero buildup amplitude, below zero for the data measured without the bias.

So it turns out that the negative charges resulting from the direct ionization of residual air between the detector and the backscatter or between the detector and buildup are indeed reaching the detector plate in the original (zero bias) experiment as was suggested by Figure 4-4. The air, and possibly the insulating tape, trapped between two electrodes (i.e. detector and grounded copper backscatter or detector and grounded copper buildup) emulate an ion-chamber. These negative charges are responsible for reducing the RIC in the measured data. As a result, the RIC in the measured data reaches a zero value at a smaller buildup thickness than expected. The 6 MV beam used in these experiments reaches a maximum dose at 1.4-1.5 cm depth in water. A simple density scaling would indicate that the depth of maximum dose in copper would occur somewhere between 0.1-0.2 cm (also see Figure 4-6). However, the RIC in the measured data for copper detector and copper buildup case in Figure 4-3 reaches zero values around 0.07 cm of buildup thickness. Beyond electronic equilibrium, a negative value for the measured RIC indicates that the detector plate receives excess negative charges. It is suggested that these negative charges are contributed by the direct ionization of the air in between plates. But the amount of air ionization should be a function of beam intensity remaining in the beam after being attenuated by the buildup material beyond the thickness that establishes electronic equilibrium. Thus, by increasing the buildup thickness further, the air ionization is reduced as the beam intensity is reduced, and the measured RIC amplitude becomes less negative as seen in Figure 4-4. It is evident from Figure 4-5, that his effect can be reduced if the buildup and backscatter are biased. Ionizations add to the measured signal amplitude when the buildup and backscatter are positively biased (+10 V) since the detector is collecting extra positive charges and more electrons are needed from the circuit to restore charge balance. Conversely, when the buildup and backscatter are negatively biased (-10 V) the detector collects extra negative charges and does not need any electrons from the circuit, in fact it introduces extra negative charges in the circuit, and the measured signal

amplitude is negative. By adding these two signals together, twice the actual RIC amplitude is obtained, with very few contributions from air ionizations. The RIC reduction curve obtained using this method actually goes to zero amplitude at the expected copper thickness needed for electronic equilibrium (which lies between 0.1-0.2 cm for copper buildup in 6 MV beam spectrum) and does not drop significantly below zero with increasing buildup thickness. It is also clear from Figure 4-5 that a 10 V bias is not enough to collect all the ions in the air gaps. Usually in the small volume ion chambers, a bias voltage of ±300V is required to reduce the recombination effects to negligible levels. The fraction of ions collected will depend on the polarity due to the difference in the mobility of positive and negative ions. Therefore, a perfect cancellation of the charge collected in the detector plates for the opposite bias voltages is not possible at 10 V bias. As a result the measured RIC in the biased experiment does not actually stay at exactly zero value at higher buildup thicknesses. It should be mentioned that the current RF cage did not allow placement of a biasing power supply that could supply 300 V, inside the RF cage due to the limited number of electrical contacts on the cage.

4.2. Conductor Thickness

Figure 4-6 shows the measured RIC amplitudes plotted against the increasing thickness of the copper detector with no buildup. The curve, thus obtained, displays a sharp increase in RIC amplitude as the detector gets thicker, up to about 0.16 cm, where the curve reaches a maximum. Beyond this point the RIC amplitude slowly decreases with increasing detector thickness.

This data behaves like a classical depth dose curve since 0.15-0.16 cm is expected to be the depth of maximum dose in copper. The initial increase in the RIC amplitude is due to an increasing number of Compton electrons being produced with increasing detector thickness, most of which leave the detector. As the detector thickness increases past the electron range, not all of the Compton electrons produced in the detector escape it anymore, and the RIC amplitude starts

to slowly decrease. Measurements agree quite well with the expected overall trend in this case.

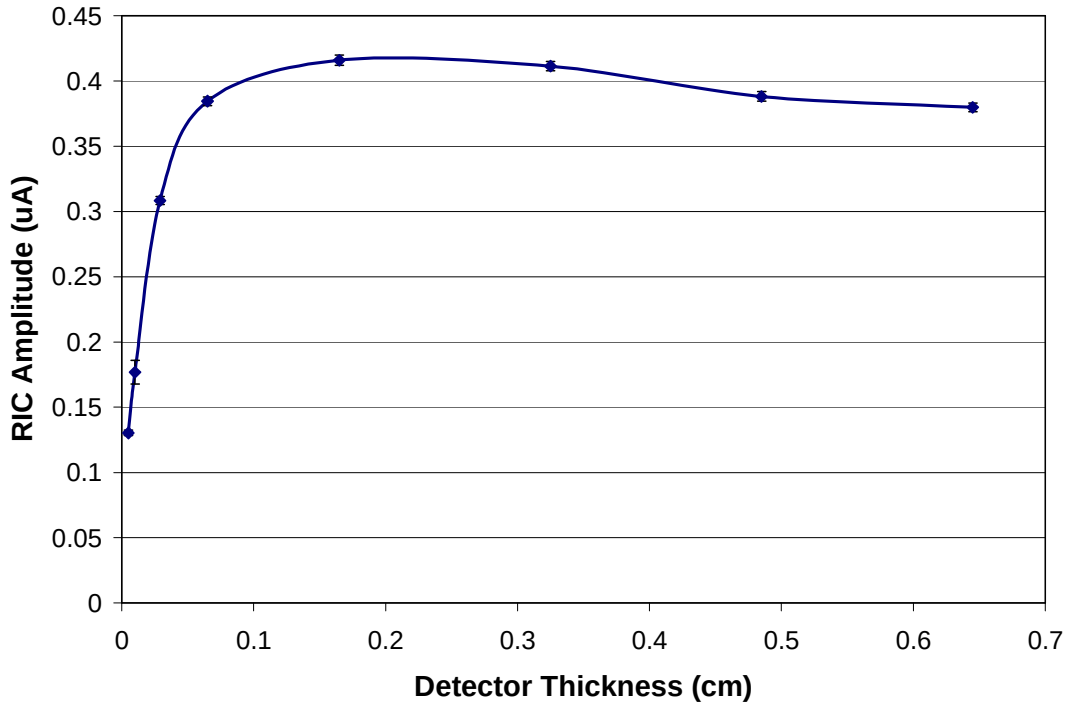

Figure 4-6: Influence of detector thickness on RIC amplitude shown for copper detector with no buildup.

4.3. Influence of Backscatter

Figure 4-7 shows the influence of the backscatter on the copper detector/copper buildup measurements. It can be clearly seen that electronic equilibrium can not be attained for the copper detector, if Styrofoam is the first material in contact with the detector in the backscatter stack.

Although almost identical, the entire RIC reduction curve obtained with Styrofoam for backscatter is shifted upwards by about 120% compared to the curve obtained with copper for backscatter. Please note that both experiments in this case were performed with a zero bias method.

The influence of the backscatter on the aluminum detector/Teflon buildup measurements is presented in Figure 4-8.

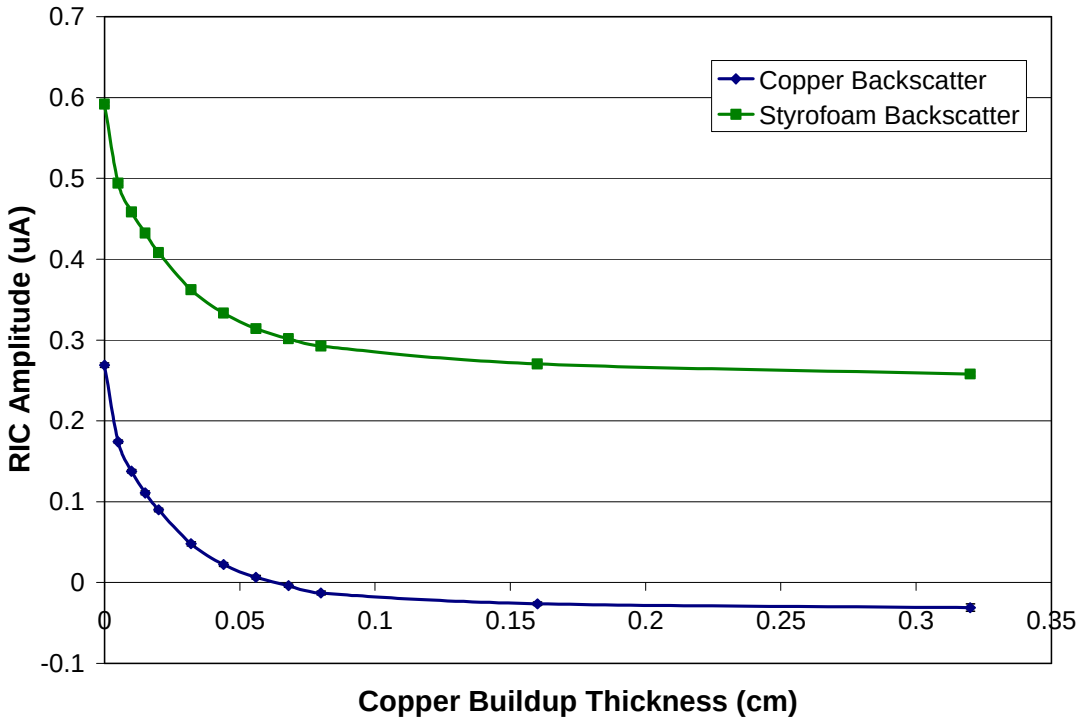

Figure 4-7: Influence of the backscatter material on RIC amplitude is shown for the copper detector/copper buildup measurements.

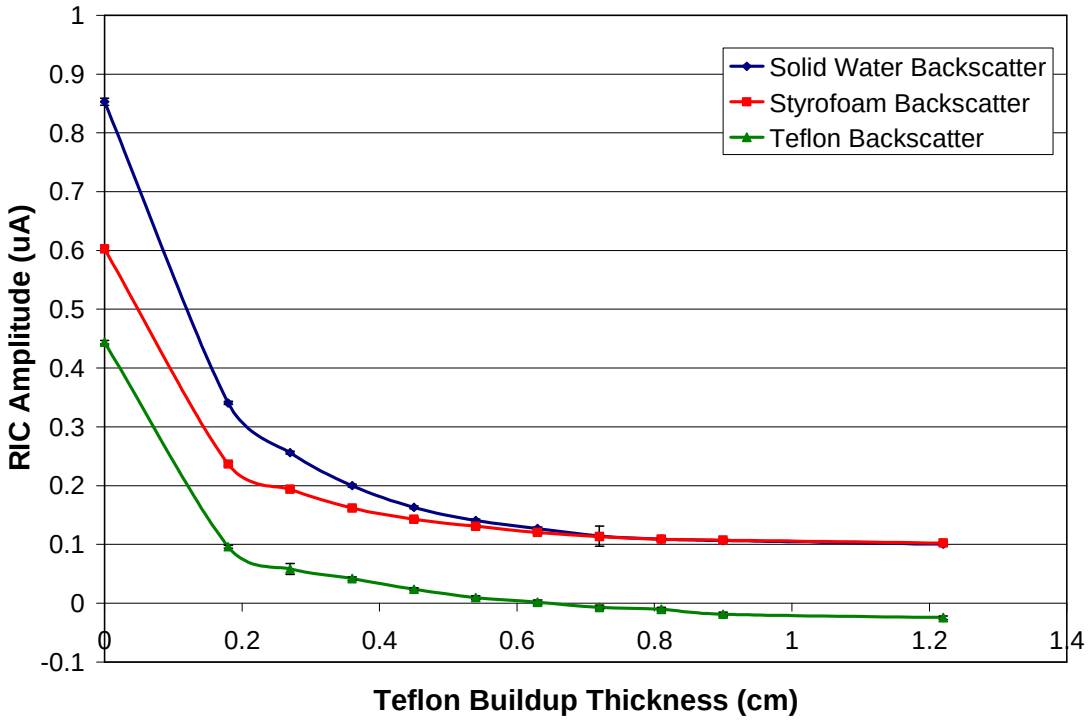

Figure 4-8: Influence of backscatter material on RIC amplitude is shown for the aluminum detector/Teflon buildup measurements.

It can be seen that an aluminum conductor with Teflon buildup is not as sensitive to the backscatter material as a copper conductor with copper buildup, and the RIC reduction curves for solid water and Styrofoam backscatters converge after about 0.7 cm of Teflon buildup. These two curves differ by less than 2% from each other for subsequent buildup thicknesses above 0.72 cm. The third curve, obtained with 2 cm of Teflon, with grounded aluminum tape on the top and on the bottom, for backscatter, exhibits the same type of behavior as the copper detector/copper buildup curve. The RIC goes to zero at about 0.63 cm of Teflon buildup, after which it keeps dropping below zero with increasing buildup thickness. This could be due to the extra ionizations collected by the aluminum detector (similar to explanation in §4.1), which is now between two grounded electrodes (grounded aluminum tape on bottom of buildup and grounded aluminum tape on top of backscatter). Note that this last set of measurements was also performed with a zero bias method.

It is clear from both Figure 4-7 and Figure 4-8 that the backscatter material plays a major role in the reduction of RIC with the help of buildup in thin conductors. Figure 4-7 shows the 0.12 mm thick copper detector to be unable to reach electronic equilibrium unless it has copper for backscatter, irrespective of how much buildup is used. The 120% jump in zero buildup amplitude of the RIC reduction curve when copper is replaced by Styrofoam indicates that overall the backscatter material was contributing a significant number of electrons to the detector. These electrons, coming from the backscatter, were replacing a part of the Compton electrons that were being knocked out of the detector by the beam. On the other hand it has been shown that for this particular setup (copper detector/copper buildup/copper backscatter) there is a contribution from ions created in the air or electrical tape surrounding the detector. These ions have been shown to work as a reverse current that decreases the RIC amplitudes for all the buildup thicknesses. With this in mind, and taking note that the data presented in Figure 4-7 was not taken with any type of bias to try to remove the effect of these ions, one might expect the copper backscatter curve to be shifted a bit higher than shown. The Styrofoam backscatter curve is expected to have higher amplitudes,

since the major electrode (the backscatter) is missing in this particular setup. In any case it does not seem feasible to build a RIC free RF coil with a copper conductor using both copper buildup and copper backscatter. The backscatter copper plates would shield the coil from receiving any signal from the patient in the MRI studies, while removing the copper backscatter and just keeping the buildup would still leave a significant residual RIC amplitude.

Figure 4-8 shows the RIC measured with the 0.54 mm thick aluminum detector and Teflon as buildup material, using three different types of backscatter. The Teflon backscatter curve has the smallest zero buildup RIC amplitude and is the only curve that goes to zero and below in this set of measurements. It is suspected that this (i.e. the negative RIC amplitude) is due to the same effect as present for the copper detector/copper buildup and backscatter case. Since the Teflon backscatter had a layer of grounded aluminum tape on the top and on the bottom, this put the aluminum detector in the same situation as the copper detector. In between two grounded electrodes (aluminum tape on bottom of buildup and aluminum tape on top of backscatter), the detector plate could be collecting ionizations from the surrounding electrical tape or air, like the copper detector was shown to do. At the same time, having a material that is so close in density for both the buildup and the backscatter, might help the RIC amplitude, in the aluminum conductor get reduced faster, than for the solid water and Styrofoam backscatter setups. This drastic reduction only happens however when the Teflon backscatter is in between grounded electrodes, which means that this particular combination of materials is also impractical for building an actual RF coil.

For the case of zero buildup thickness, the RIC amplitude for the Styrofoam backscatter is lower than for the solid water backscatter as seen in Figure 4-7. This may be caused by backscattered photons resulting from the Compton interactions. These photons are knocking out more electrons from the detector. Since the Compton interaction cross section depends on the density of material, it could be assumed that there are more backscattered photons in the case of the solid water backscatter than the Styrofoam. Therefore, the RIC signal

for Styrofoam backscatter material is smaller than for the solid water backscatter. This difference between the two curves disappears almost entirely after about 0.7 cm of buildup is placed on top of the detector, since the number of backscattered photons produced in the solid water has decreased, and there are enough electrons coming from the buildup to make the difference between the two buildups negligible.

Although an aluminum coil built with Teflon for buildup and Teflon for backscatter seems to be ideal in reducing the RIC to zero values, the need for the grounded electrodes on the top and bottom of the backscatter Teflon, would shield the coil from the inside (or the patient side) rendering it useless. However, both the solid water (simulating as if the coil is in contact with the patient) and the Styrofoam (simulating a small gap between the coil and the patient) backscatter help reduce the RIC to small levels. These two types of structures will not interfere with the coil's ability to measure MRI's free induction decay while imaging since there is no need for the grounded electrodes on the backscatter side.

4.4. Aluminum Surface Coil

Reducing the RIC in an aluminum surface coil works quite well as seen in Figure 4-9. The initial (zero buildup) RIC amplitude is small, compared to the other measurements using aluminum for a detector, despite the surface coil being closer to the radiation source compared to plate detectors in the first set of experiments, due to the much smaller irradiated surface area. The RIC amplitude is reduced by 92% of its original value by only 0.9 cm of Teflon buildup.

This set of results indicates that Teflon is a suitable material for reducing RIC in actual coils with an aluminum conductor. It should be noticed that the backscatter material (Styrofoam plus solid water) was not the same as for the aluminum detector measurements in this case. Despite this mismatch between buildup, detector and backscatter materials, the Teflon buildup is successful in reducing the RIC to small values. Thus the aluminum conductor RF coil is not as sensitive to the backscatter material as a copper conductor RF coil might be, as

was also suggested by the data presented in Figure 4-8 and explained in the previous section. Overall, out of all the materials studied, aluminum for the coil conductor and Teflon for the buildup are well suited for reducing RIC to negligible levels in RF coils.

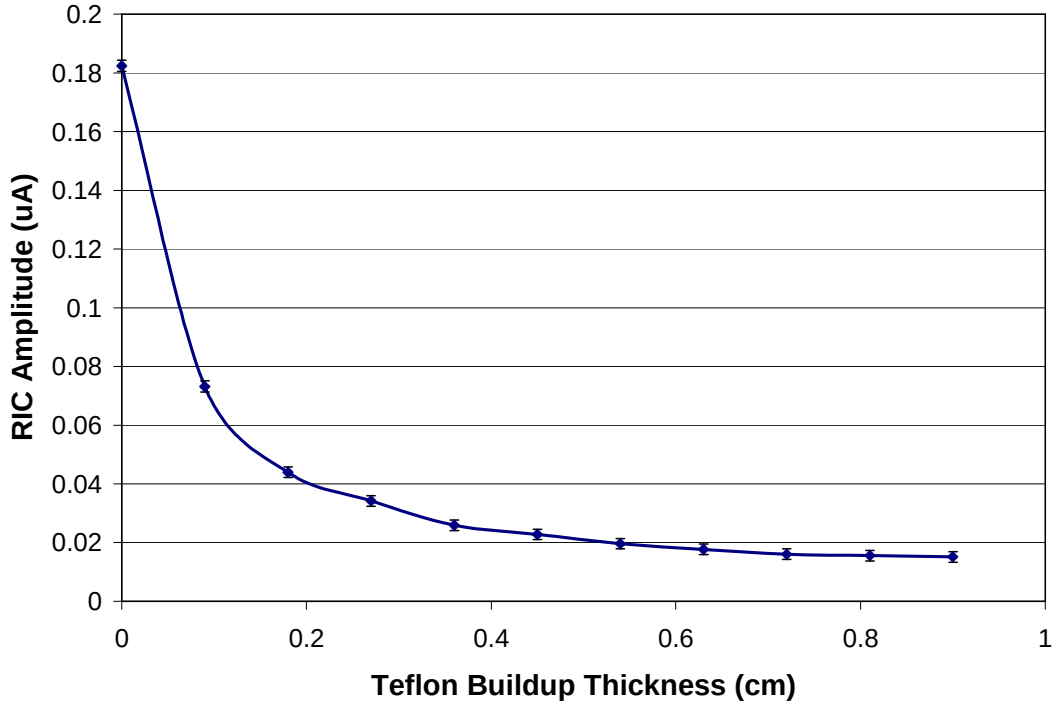

Figure 4-9: RIC reduction in an aluminum surface coil is shown as a function of Teflon buildup thickness.

4.5. Skin Dose Measurements

Figure 4-10 and 4-11 show the percent depth doses (PDD) for the emulated (see §3.3) copper conductor and aluminum conductor RF coils respectively. The PDDs are measured at various depths in the solid water phantom. The so called regular PDD (10 x 10 cm^2 field size, 6 MV source with SSD = 100 cm), is compared to the PDD's obtained with the emulated coil materials in the beam, placed at distances ranging from 0-10 cm from the surface of the solid water phantom.. All of the curves were normalized to the 100% of the regular PDD curve (~ 1. 5 cm depth in solid water) for comparison purposes.

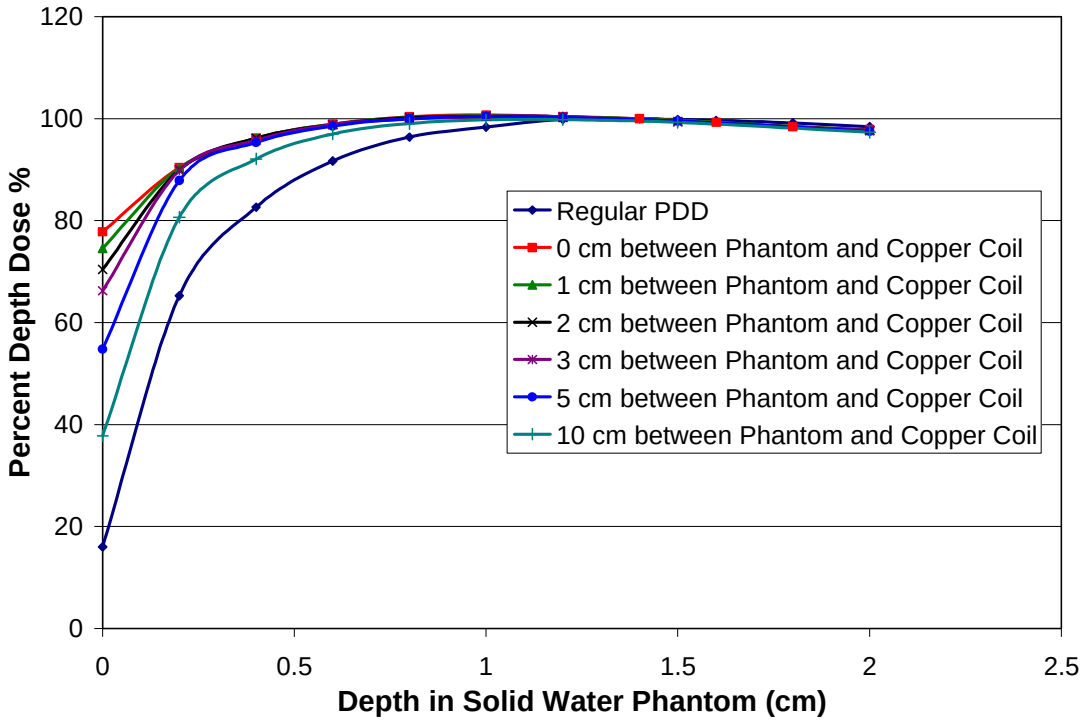

Figure 4-10: Percent depth dose measurements in solid water with regular emulated copper coil materials with no buildup, placed at various distances from the solid water phantom surface.

Although the densities of the two conductors are substantially different ($\rho_{Al} = 2.7\, g/cm^3$; $\rho_{Cu} = 8.9\, g/cm^3$)the two graphs look almost identical. The copper conductor coil material has only about 1% higher skin dose than the aluminum conductor coil material, for distances ranging from 0-3 cm between the coil materials and the surface of the phantom. For 5 cm and 10 cm distances between coil and phantom there are no significant differences between the PDD curves obtained with the two different coil conductors. This is due to the very thin conductors that were used (0.06 mm thick aluminum and 0.08 mm thick copper), which are actually common for certain types of RF coils. Despite the significant difference in density of the two conductors, their thicknesses were too small for the photon beam to produce substantially more secondary electrons or to be more attenuated in the copper conductor than in the aluminum conductor. As the distance between the coil materials and the phantom increased, some of those few extra electrons that do get produced in the copper conductor scatter laterally and

no longer contribute to the dose measured by the ion chamber. Essentially, adding the coil material right on top of the solid water phantom will start creating a partial electronic equilibrium, and move the depth of maximum dose closer to the surface of the phantom. As the coil materials are moved away from the surface of the solid water phantom, this partial electronic equilibrium is going to be lost, the depth of maximum dose will increase again and the dose at the surface of the phantom will go down. Since the beam is not appreciably attenuated by the RF coil materials, whether the copper or aluminum conductor is used, all the PDD curves converge close to the depth of maximum dose in water. This happens for all the separation distances between the coil materials and the surface of the solid water phantom, because most of the extra secondary electrons produced in the coil materials will have either stopped and deposited their dose by the time the depth of maximum dose is reached or scattered laterally.

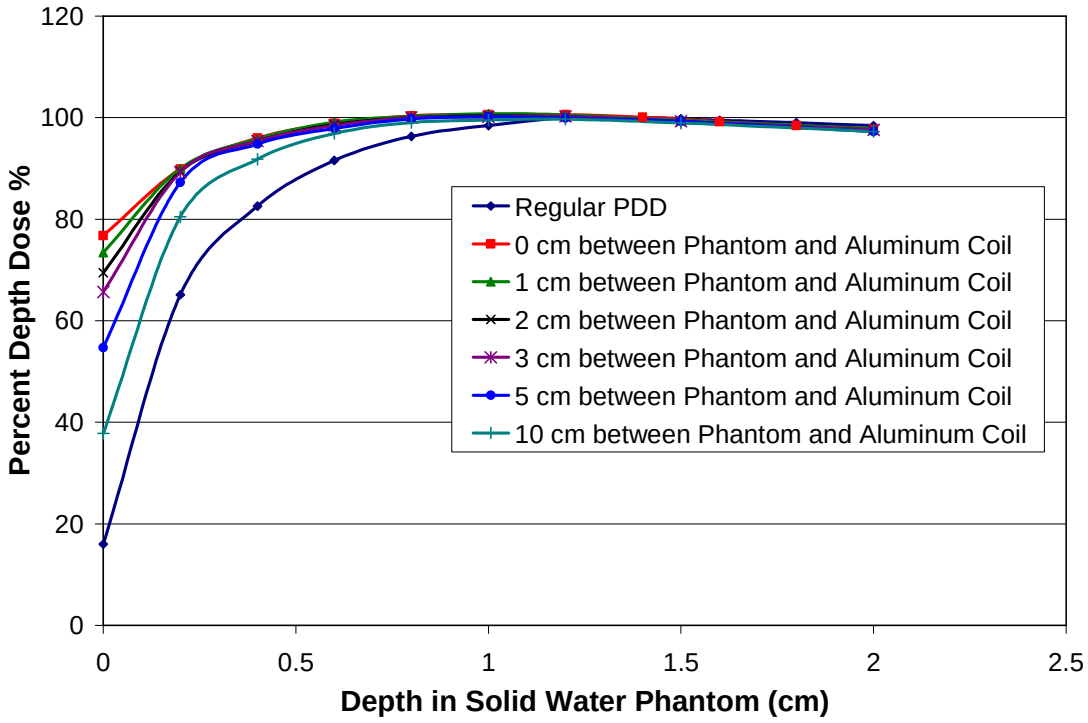

Figure 4-11: Percent depth dose measurements in solid water with a regular emulated aluminum coil materials with no buildup, placed at various distances from the solid water phantom surface.

In both cases the skin dose increases significantly though, from about 16% (when no coil material is present in the beam) to almost 80% of the maximum dose, for the case when the coil is right against the phantom surface. As the gap between coil materials and the phantom surface is increased, the skin dose is reduced reaching about 38% of the maximum dose for a 10 cm distance between phantom and coil materials. It is also obvious that the coil materials only affect the surface dose and the build up region of the PDDs, as the PDD curves converge at ~ 1.2 cm depth in the solid water phantom. One thing to note would be that this would be the expected increase in skin dose for a patient irradiated through an RF coil, right under the RF coil conductor, and not for the entire area covered by the RF coil.

Figure 4-12 shows the PDDs for a reduced RIC aluminum conductor RF coil with 0.9 cm of Teflon buildup placed in the radiation beam at various distances from the phantom, compared to the regular PDD with no coil material in the beam.

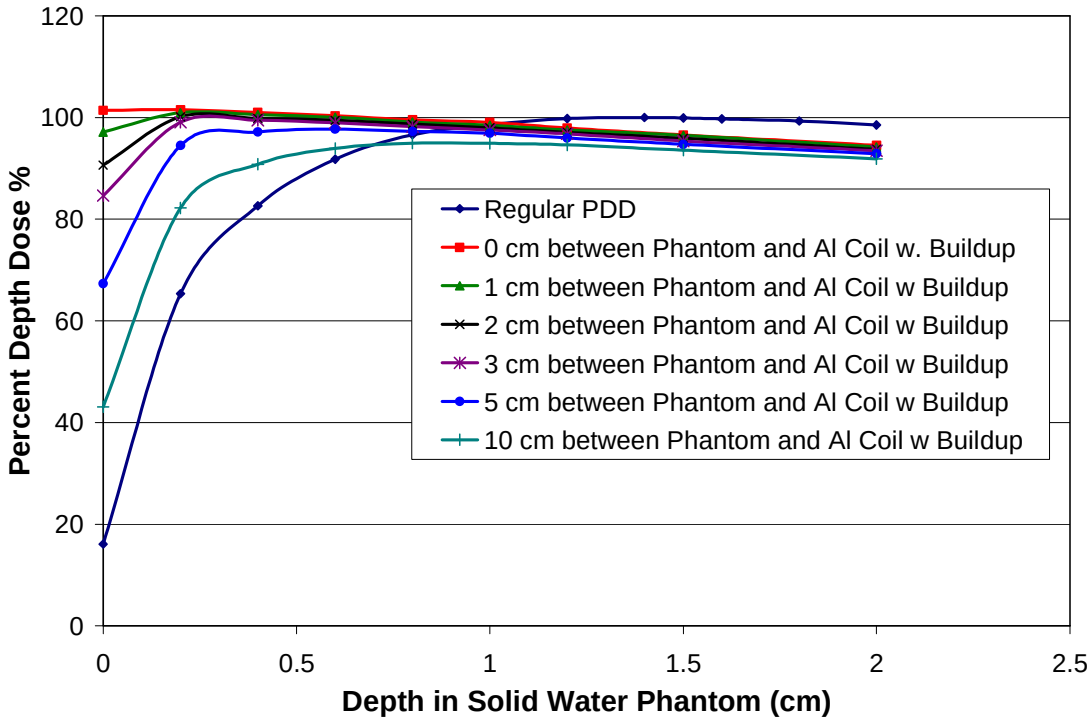

Figure 4-12: Percent depth dose measurements for reduced RIC aluminum coil materials with buildup, at various distances from the solid water phantom.

As before, all of the data points have been normalized to the 100% point of the regular PDD curve for comparison purposes. The surface skin dose increases to 101% of the maximum dose of the regular PDD, when this type of RF coil is placed in direct contact with the phantom. Even with the coil materials placed 5 cm away from the surface of the phantom, the skin dose is still about 67% of the maximum dose, and with a 10 cm air gap it falls to 43%. The PDD curves don't seem to converge anymore (at least not within the measured range of 2 cm), and for a depth greater than about 0.9 cm in the phantom the dose is lower for all the curves obtained with coil material in the beam than for the regular PDD.

Thus, the increase in surface dose is even more significant than before. Since the goal of placing Teflon on top of the aluminum conductor was to re establish electronic equilibrium in the conductor, the skin sparing effect of high energy photons, based on electronic equilibrium not being established at the surface, is completely removed. This is obvious from the fact that for the PDD measured with the reduced RIC aluminum coil right on top of the solid water phantom the surface dose is virtually the highest dose of that particular PDD curve. As the emulated RF coil is taken further and further from the surface of the solid water phantom the surface dose gradually drops, however even at a distance of 10 cm from the patient the skin dose is still at 43% of the maximum dose. The entire depth dose profile is now affected, not just the buildup region, as the beam actually does get appreciably attenuated in the Teflon buildup and coil materials, and the PDDs do not all converge anymore.

It is known that surface dose measurements, with fixed separation parallel plate ion chambers, are prone to errors. To remove these errors introduced by the fixed separation of the electrodes, an extrapolation chamber is usually used. Since one was not available for the measurements presented here, the surface dose measured with an extrapolation chamber in Ref [3] was compared to the surface dose measured with the Capintec PS-033 chamber. The only difference in terms of setup between [3] and the measurements presented here was the Varian Clinac 2500 that was used for the extrapolation chamber measurements in Ref [3]. For a

field size of 10 cm by 10 cm and an SSD of 100 cm, the percent of maximum ionization reported in [3] is slightly above 15% for the surface of the phantom. The measurements taken with the Capintec PS-033 during the course of this work, yielded for the same experimental conditions, between 16% and 16.1% of maximum ionization at the surface of the phantom (the so called regular or standard PDD). Thus the deviation in the surface dose measurements caused by the fixed separation parallel plate chamber presented herein should be around 1%.

Figure 4-13 compares some of the PDD measurements taken with the Capintec 192A Digital Dosimeter, which do not take the polarity effect into account, with PDD measurements taken with a PTW Unidos E electrometer/dosmeter, which do take the polarity effect into account, for the reduced RIC aluminum conductor RF coil.

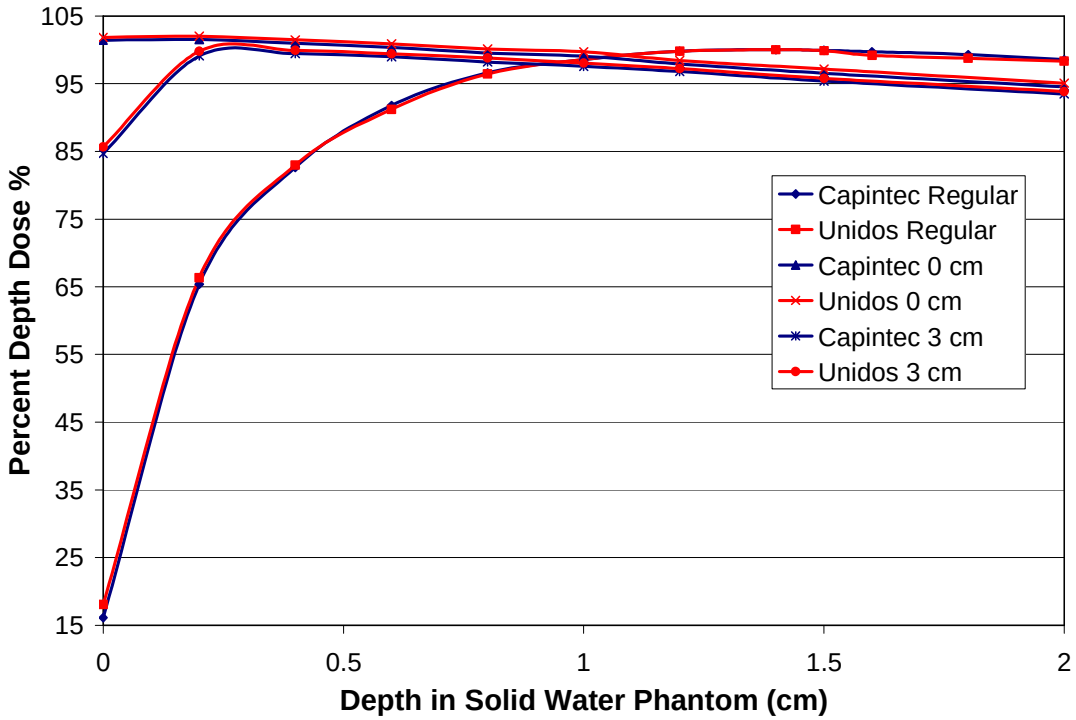

Figure 4-13: Estimating the error introduced by the polarity effect. The Capintec electrometer measurements (polarity effect not taken into account) are compared to Unidos electrometer measurements (polarity effect taken into account).

Specifically the regular PDD measurements were redone, as well as the 0 and 3 cm separation between coil materials and surface solid water phantom.

Overall the difference is only at most 1% higher values when the polarity effect is accounted for. One exception is the surface dose of the regular PDD which is about 2% higher when the polarity effect is removed.

4.6. Linac vs. Linac-MR RF Coil Measurements

Figure 4-14 presents the typically measured time dependent RIC of the black RF coil without a magnetic field, taken on a Varian 600C clinical linac, and Figure 4-15 shows the same curve for the same RF coil with a transverse magnetic field (~ 0.22 T) present, taken on the prototype linac-MR system. The overall shape of the two curves is similar suggesting that the shape of the RIC pulse is particular to the RF coil circuitry, as suggested in [4] or possibly to the conductor shape as well (flat conductor vs. hollow pipe). The time duration of the RIC pulses is about the same as well in the two cases presented, suggesting this to depend on the magnetron pulse length which is the same for both the Varian 600C linac and the linac-MR system. The amplitude of the RIC pulse measured with the magnetic field present is about 2.5 times lower than the amplitude of the pulse measured without the magnetic field. This difference in overall amplitude of the two pulses could be, as stated before, due to a lower dose per pulse of the linac-MR prototype compared to the Varian 600C clinac. Also the RIC signal in the presence of the magnetic field seems to have a low-frequency ringing following the main pulse which is not present for the trace acquired on the clinical linac, without a magnetic field. Further investigation is needed to be able to conclude for certain that this ringing is due to the magnetic field presence or to other factors. However these measurements show that whether with or without a magnetic field present, a RIC on the order of microamperes is induced in an irradiated RF coil.

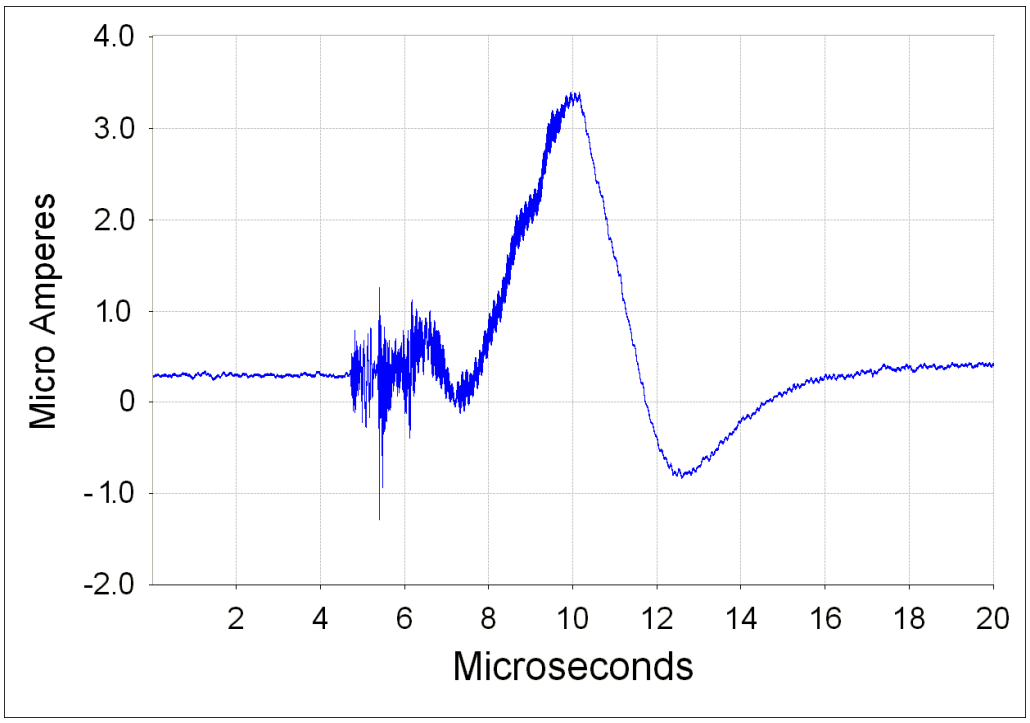

Figure 4-14: Black coil RIC trace obtained on a Varian 600C clinical linac.

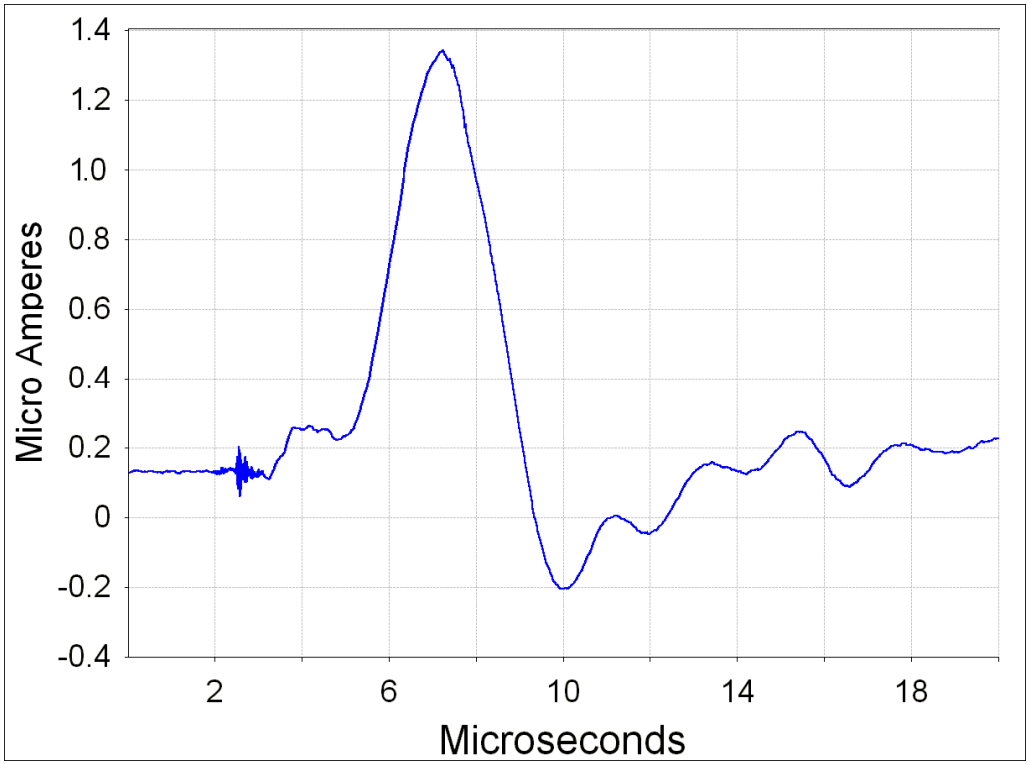

Figure 4-15: Black Coil RIC trace in transverse magnetic field obtained on prototype linac-MR system.

References:

1. G.M. Sessler, “Introduction”, *Topics in Applied Physics Volume 33: Electrets*, Editor: G.M. Sessler, Springer-Verlag Berlin Heidelberg New York, 1980.
2. B.Gross, “Radiation-Induced Charge Storage and Polarization Effects”, *Topics in Applied Physics Volume 33: Electrets*, Editor: G.M. Sessler, Springer-Verlag Berlin Heidelberg New York, 1980.
3. B.J. Gerbi and F.M. Khan, *Measurement of dose in the buildup region using fixed-separation plane-parallel ionization chambers*, Med. Phys. **17** (1), 17 – 26, 1990.
4. B. Burke, B. G. Fallone, and S. Rathee, *Radiation induced currents in MRI RF coils: application to linac/MRI integration*, Phys. Med. Biol., **55**, 735-746, 2010.

5. Discussion

Effect of RIC on MR Images

Although a more thorough analysis of the effect of RIC in RF coils is given in a companion thesis, a brief speculative description is given here. In the most favorable operational scenario, the pulsed irradiation and MR imaging of the patient are likely occurring asynchronously and independently of each other. In this case, the RIC pulses are likely to fall within the data acquisition (i.e. during the switching of the read gradient) of the MRI. Since the signal data acquired in MRI is the Fourier transform of the sample's spin density, the image space is obtained from the data space (also known as the k-space) through the inverse Fourier transform. Also, the data acquisition corresponding to each line in k-space in MRI occurs with a fixed period (i.e. repetition time) and the linac produces radiation pulses at regular time intervals, thus the RIC pulses will show up as lines in the k-space. One may also see multiple lines in the k-space if the data acquisition window is larger in time to encompass more than one radiation pulse. One immediate effect of these lines is to create a background noise signal in the MR images reconstructed with the conventional inverse 2-D Fourier transform method. The magnitude of this noise signal will depend on the magnitude of the RIC pulse. Therefore, if the RIC in the coil is reduced to small levels using the appropriate coil design, the magnitude of this background noise can also be reduced.

6. Conclusions and Future Work

The work presented in this thesis demonstrates that the RIC can be reduced with the appropriate combination of coil conductor and buildup. The results indicate that the best combination of materials is about 1 cm of Teflon wrapped around an aluminum RF coil. In this type of coil there would be no need for any type of backscatter for the aluminum conductor, since the buildup alone would suffice to essentially eliminate the radiation induced currents. Future work will assess the effect of RIC on the signal to noise ratio in MR images to determine if such steps are necessary in coil design. Since the Teflon buildup needs to be sandwiched between two grounded electrodes, an investigation, into whether a coil built using the above principles can function properly in MRI imaging experiments, is yet to be done.

The skin dose was found to increase significantly due to the placement of a reduced RIC RF coil (aluminum conductor with Teflon buildup) in the treatment beam. Even for a regular coil, whether built with a copper or aluminum conductor, the skin dose increase is still significant (from 16% of maximum dose to almost 40 % of maximum dose). These effects have to be taken into account during the treatment planning process, or a solution that would allow the patient to be irradiated in such a way that the high energy beam will not have to go through any of the RF coil materials has to be found.

It has also been shown that the RIC appears in an RF coil both with and without a magnetic field present. Further investigation is needed to find out the effects the magnetic field presence has on the RIC in RF coils and on the RIC reduction with buildup in RF coil materials.

7. Bibliography

1. O. Glasser, *Wilhelm Conrad Rontgen and The Early History of the Roentgen Rays*, Charles C Thomas, Springfield Illinois, pp 1 – 28, 1934.
2. J. Bernier, E.J. Hall, and A. Giaccia, *Radiation oncology: a century of achievements*, Nature Reviews Cancer **4**, 737 – 747, 2004.
3. C.A. Perez, L.W. Brady, J.L. Roti "Overview" *Principles and Practice of Radiation Oncology 3rd Edition*, Editors: C.A. Perez and L.W. Brady, Philadelphia, PA: Lippincott-Raven, pp.1 – 78, 1998.
4. J. Van Dyk *The Modern Technology of Radiation Oncology*, Editor: J. Van Dyk, Medical Physics Publishing, Madison, Wisconsin, pp. 1- 18, 1999.
5. E. Lysholm, *Apparatus for the production of a narrow beam of rays in treatment by radium at a distance*, Acta Radiologica, **2**, 516 – 519, 1923
6. G. Failla, *An objective method for the administration of x-rays*, Acta Radiologica, **4,** 85 – 128, 1925.
7. J. Van Dyk *The Modern Technology of Radiation Oncology, Volume 2*, Editor: J. Van Dyk, Medical Physics Publishing, Madison, Wisconsin, pp. 1- 29, 2005.
8. D. Verellen, M. De Ridder, N. Linthout, K. Tournel, G. Soete, G. Storme *Innovations in image-guided radiotherapy*, Nature Reviews. Cancer **7,** 949 – 960, 2007.
9. L.A. Dawson and D.A. Jaffray *Advances in Image-Guided Radiation Therapy*, Journal of Clinical Oncology **25(8)** 938-946, 2007.

10. L.A. Dawson, M.B. Sharpe *Image-guided radiotherapy: rationale, benefits, and limitations*, Lancet Oncol., **7**, 848-858, 2006.
11. H. Shirato, S. Shimizu, K. Kitamura, T. Nishioka, K. Kagei, S. Hashimoto, H. Aoyama, T. Kunieda, N. Shinohara, H. Dosaka-Akita, and K. Miyasaka, *Four-dimensional treatment planning and fluoroscopic real-time tumor tracking radiotherapy for moving tumor*, Int. J. Radiation Oncology Biol. Phys., **48**, 435-442, 2000.
12. J Pouliot, A Bani–Hashemi, J Chen, et al. *Low-dose megavoltage cone-beam CT for radiation therapy*. Int J Radiat Oncol Biol Phys.;61(2):552–560, 2005.
13. T. R. Mackie, T. Holmes, S. Swerdloff, P. Reckwerdt, J. O. Deasy, J. Yang, B. Paliwal, and T. Kinsella, *Tomotherapy - a new concept for the delivery of dynamic conformal radiotherapy*, Medical Physics, **20**, 1709-1719, 1993.
14. A.P. Shah, K.M. Langen, K.J. Ruchala, A. Cox, P.A. Kupelian, and S.L. Meeks *Patient Dose from Megavoltage Computed Tomography Imaging*, Int. J. Radiation Oncology Biol. Phys., **70 (5)**, 1579–1587, 2008
15. J. Lattanzi, S. McNeeley, W. Pinover, E. Horwitz, I. Das, T.E. Schultheiss, and G.E. Hanks, *A comparison of daily CT localization to a daily ultrasound-based system in prostate cancer*. Int. J. Radiat. Oncol. Biol. Phys. **43**, 719–725, 1999.
16. H. Johnston, M. Hilts, W. Beckham, E. Berthelet, *3D ultrasound for prostate localization in radiation therapy: A comparisonwith implanted fiducial markers*, Medical Physics, **35 (6)**, 2403 – 2413, 2008.
17. B. G. Fallone, B. Murray, S. Rathee, T. Stanescu, S. Steciw, S. Vidakovic, E. Blosser, and D. Tymofichuk, *First MR images obtained during megavoltage photon irradiation from a*

prototype integrated linac-MR system, Medical Physics, **36**, 2084-2088, 2009.

18. B. W. Raaymakers, J. J. W. Lagendijk, J. Overweg, J. G. M. Kok, A. J. E. Raaijmakers, E. M. Kerkhof, R. W. van der Put, I. Meijsing, S. P. M. Crijns, F. Benedosso, M. van Vulpen, C. H. W. de Graaff, J. Allen, and K. J. Brown, *Integrating a 1.5 T MRI scanner with a 6 MV accelerator: proof of concept*, Phys. Med. Biol., **54**, N229-N237, 2009.
19. J. F. Dempsey, D. Benoit, J. R. Fitzsimmons, A. Haghighat, J. G. Li, D. A. Low, S. Mutic, J. R. Palta, H. E. Romeijn, and G. E. Sjoden, *A Device for Realtime 3D Image-Guided IMRT*, Int. J. Radiat. Biol., **63**, S202-S202, 2005.
20. A. J. E. Raaijmakers, B. W. Raaymakers, and J. J. W. Lagendijk, *Experimental verification of magnetic field dose effects for the MRI-accelerator*, Phys. Med. Biol., **52**, 4283-4291, 2007.
21. A. J. E. Raaijmakers, B. W. Raaymakers, and J. J. W. Lagendijk, *Magnetic-field-induced dose effects in MR-guided radiotherapy systems: dependence on the magnetic field strength*, Phys. Med. Biol., **53**, 909-923, 2008.
22. A. J. E. Raaijmakers, B. W. Raaymakers, S. van der Meer, and J. J. W. Lagendijk, *Integrating a MRI scanner with a 6 MV radiotherapy accelerator: impact of the surface orientation on the entrance and exit dose due to thetransverse magnetic field*, Phys. Med. Biol., **52**, 929-939, 2007.
23. C. Kirkby, B. Murray, S. Rathee, and B. G. Fallone, *Lung dosimetry in a linac-MRI radiotherapy unit with a longitudinal magnetic field*, Med. Phys., **37**, 4722-4732, 2010.
24. C. Kirkby, T. Stanescu, S. Rathee, M. Carlone, B. Murray, and B. G. Fallone, *Patient dosimetry for hybrid MRI-radiotherapy systems*, Med. Phys., **35**, 1019- 1027, 2008.

25. C. Kirkby, T. Stanescu, and B. G. Fallone, *Magnetic field effects on the energy deposition spectra of MV photon radiation*, Phys. Med. Biol., **54**, 243-257, 2009.
26. B. Burke, M. Lamey, S. Rathee, B. Murray, and B. G. Fallone, *Radio frequency noise from clinical linear accelerators*, Phys. Med. Biol., **54**, 2483- 2492, 2009.
27. B. Burke, B. G. Fallone, and S. Rathee, *Radiation induced currents in MRI RF coils: application to linac/MRI integration*, Phys. Med. Biol., **55**, 735-746, 2010.
28. M. Lamey, B. Burke, E. Blosser, S. Rathee, N. De Zanche, and B. G. Fallone, *Radio frequency shielding for a linac-MRI system*, Phys. Med. Biol., **55**, 995- 1006, 2010.
29. F.H. Attix, *Introduction to Radiological Physics and Radiation Dosimetry*, John Wiley & Sons, 1986.
30. http://www.nist.gov/pml/data/xcom/index.cfm
31. H.E. Johns, J.R. Cunningham, *The Physics of Radiology Fourth Edition*, Charles C Thomas, Springfield, Illinois, 1983.
32. A. Nahum, *Handbook of Radiotherapy Physics Theory and Practice*, Edited by P. Mayles , A. Nahum , and J. C. Rosenwald, Taylor & Francis 2007, pp 89 – 115.
33. H.E. Johns, A. Aspin, and G.G. Baker, *Currents Induced in the Dielectrics of Ionization Chambers through the Action of High-Energy Radiation*, Radiation Research **9**, 573 – 588, 1958.
34. R.A. Meyer, F.L. Bouquet, and R.S. Alger, *Radiation-induced conductivity in polyethylene and Teflon*, J. Appl. Phys. **27**, 1012 – 1018, 1956.
35. B. Gross, *Compton Dosimeter for Measurement of Penetrating X-Rays and Gamma Rays*, Radiation Research, **14**, 117 – 130, 1961.
36. Abdel-Rahman, J.P Seuntjens., F Verhaegen., Podgorsak E.B, *Radiation induced currents in parallel plate ionization*

chambers: Measurement and Monte Carlo simulation for megavoltage photon and electron beams, Med. Phys. **33** (9), 3094 – 3104, 2006.

37. G.M. Sessler, "Introduction", *Topics in Applied Physics Volume 33: Electrets*, Editor: G.M. Sessler, Springer-Verlag Berlin Heidelberg New York, 1980.
38. B. Gross, "Radiation-Induced Charge Storage and Polarization Effects", *Topics in Applied Physics Volume 33: Electrets*, Editor: G.M. Sessler, Springer-Verlag Berlin Heidelberg New York, 1980.
39. C.J. Karzmark, and N.C. Pering, *Electron Linear Accelerators for Radiation Therapy: History, Principles and Contemporary Developments*, Phys. Med. Biol., **18**, 321-354, 1973.
40. http://www.lbagroup.com/technology/faraday-cages.php, Copyright 2009. LBA Group, Inc.
41. http://www.edmundoptics.com/images/imagelib/ds59179.pdf, EO-59-179_2/R 2/SP/11Oct06.
42. B.G Fallone. and E.B Podgorsak, *Production of foil electrets by ionizing radiation in air*, Physical Review B **27** (4), 2615 – 2618, 1983.
43. B.G Fallone. and E.B Podgorsak, *Dynamics of radiation-induced charging and discharging of foilelectrets*, Physical Review B **27** (8), 5062 – 5065, 1983.
44. http://www.nist.gov
45. B.J. Gerbi and F.M. Khan, *Measurement of dose in the buildup region using fixed-separation plane-parallel ionization chambers*, Med. Phys. **17** (1), 17 – 26, 1990.